ABSTRACT

Title of Document: QUANTITATIVE PREDICTION OF TIP-SAMPLE REPULSIVE FORCES AND SAMPLE DEFORMATION IN TAPPING-MODE FREQUENCY AND FORCE MODULATION ATOMIC FORCE MICROSCOPY

Joshua C. Crone, Master of Science, 2008

Directed By: Assistant Professor Santiago Solares,
Department of Mechanical Engineering

Dr. Peter Chung,
U.S. Army Research Laboratory

The ability to predict sample deformation and the resultant interaction forces is a vital component to preventing sample damage and acquiring accurate height traces in atomic force microscopy (AFM). By using the recently developed frequency and force modulation (FFM) control scheme, a prediction method is developed by coupling previously developed analytical work with numerical integration of the equation of motion for the AFM tip. By selecting a zero resonance frequency shift, the sample deformation is found to depend only on those parameters defining the tip-sample interaction forces. The results are represented graphically and through a multiple regression model so that the user can predict the tip penetration and maximum repulsive force with knowledge of the maximum attractive force and steepness of the repulsive regime in the tip-sample interaction force curve. The prediction model is shown to be accurate for a wide range of imaging conditions.

QUANTITATIVE PREDICTION OF TIP-SAMPLE REPULSIVE FORCES AND
SAMPLE DEFORMATION IN TAPPING-MODE FREQUENCY AND FORCE
MODULATION ATOMIC FORCE MICROSCOPY

By

Joshua C. Crone

Thesis submitted to the Faculty of the Graduate School of the
University of Maryland, College Park, in partial fulfillment
of the requirements for the degree of
Master of Science
2008

Advisory Committee:
Assistant Professor Santiago Solares, Chair
Professor Balakumar Balachandran
Associate Professor Hugh Bruck
Dr. Peter Chung

To my parents,

Charles and Susan Crone

Acknowledgements

Table of Contents

List of Tables

List of Figures

1 Introduction

1.1 *Brief Description of Work*

The focus of this thesis is on developing a method to quantitatively predict the sample deformation and maximum tip-sample repulsive force experienced during atomic force microscopy operation. The mode of operation for this study is frequency and force modulation with a resonance frequency shift setpoint of zero. However, the same findings can be applied to the more common mode, frequency modulation, if operated in tapping mode with a resonance frequency shift setpoint of zero. Extensive work has been conducted on relating the tip-sample interaction forces and other imaging parameters to the shift in resonance frequency [1-6]; however, the relationship between these imaging parameters and the resultant tip penetration has remained unexplored. The primary need for a method to reliably predict sample deformation is for the prevention of sample damage in soft samples. Post-processing of the AFM image in which the sample deformation is accounted for could also lead to increased accuracy of the height trace when imaging materials of different tip-sample interaction forces.

In the following sections, an overview of the atomic force microscope, the modes of operation, and other relevant background information is provided. Following this background information, the methods used for determining tip penetration and maximum repulsive force are provided along with the analysis of the prediction method. It will be demonstrated that quantitative predictions can be accomplished with knowledge of only the tip-sample interaction forces. Some potential applications of these predictions are proposed along with a discussion of related discoveries which require further

investigation. This thesis concludes with an appendix containing the experimental work that has been completed towards achieving experimental FFM implementation. Throughout this document the term free resonance frequency refers to the fundamental cantilever eigenfrequency, in the absence of tip-sample interaction forces.

1.2 *AFM History*

As the scale of scientific research and technology continues to decrease in size, the demand for improved tools to accurately obtain information regarding nanoscale samples continues to increase. The atomic force microscope (AFM) is one such tool that has enabled drastic improvements in the ability to image, characterize, and manipulate material on the nanoscale. Motivated by the inability to achieve high resolution images of insulated surfaces, the AFM was invented by Binning *et al* in 1986 [7]. Over the last two decades, the AFM has been transformed into a vital tool for many aspects of research within nanotechnology. Now, AFM is used in a wide variety of applications including true atomic resolution images [8-11], material characterization [12-16], and nanoscale manipulation [17-20].

Until 1986, the stylus profilometer provided the best three-dimensional images of non-conducting samples. However, the lateral resolution of 1000 Å and vertical resolution of 10 Å was significantly lower than that of the scanning tunneling microscope (STM) and prevented one from imaging nanoscale features accurately. Despite the higher resolution, the STM has a different inherent limitation as it can only image conducting samples. With the introduction of the AFM, the attainable resolution dropped to 30 Å in the lateral direction and 0.1 Å in the vertical direction for both conducting and

non-conducting samples. Since its invention, advances have been made in all phases of AFM usage, ranging from the material and equipment used to the modes of operation.

2 Background Information

2.1 *What is an AFM?*

While the equipment used and operational procedures of AFMs can vary considerably, depending on the intended purpose and brand, the core principles and apparatus remain the same. The AFM is centered around a microscale cantilever with a sharp tip at the free end. The tip, which can have a radius of curvature ranging from a few nanometers to many microns, is available in a wide variety of geometric shapes. The motion of the cantilever base and sample scanner are most often controlled by using piezo tubes. In dynamic modes, the AFM tip can be excited through various means including magnetic excitation, acoustic excitation, or base excitation via piezo tubes. The motion of the tip is generally measured by using an optical lever system, in which a laser reflects off the edge of the cantilever onto an array of photodiodes. The main components of a typical AFM are illustrated in Figure 2.1.

Both the vertical and lateral motion of the tip are measured in volts with photodiodes and then translated into distance measurements. This conversion is completed by using the predefined sensitivity parameters of the hardware and the sensitivity associated with the specific cantilever-laser alignment. The distance measurements are then either used to determine the cantilever deflection or fit to a sine curve in order to calculate the amplitude, frequency and phase of oscillation. The necessary adjustments are then made by the AFM controller, depending on the mode of

operation in use. The information gathered from this system is then sent to a computer, which is able to reconstruct a three-dimensional image of the scanned sample or provide force measurements for various characterization and manipulation techniques.
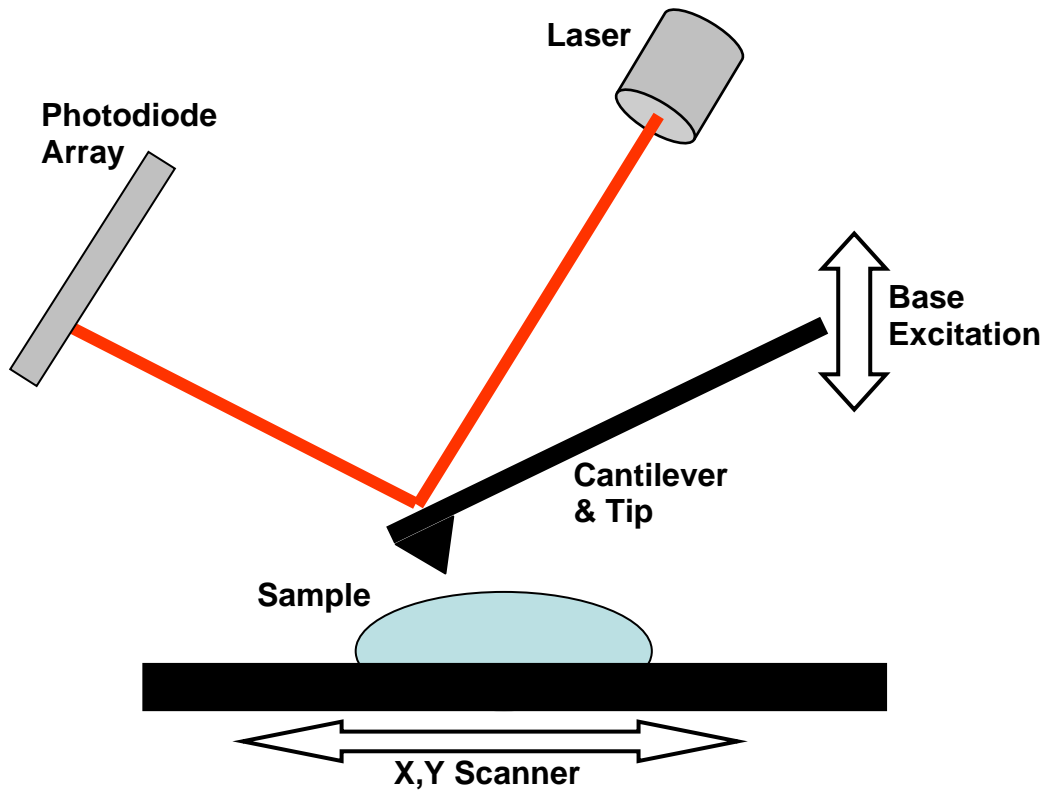
Figure 2.1 - Diagram of main components of an AFM

2.2   *Modes of Operation*

2.2.1   Contact Mode

When first invented, AFMs were only operated in what is referred to as contact mode. In contact mode, the probe is always touching the sample. As the probe moves laterally along the x and y directions, the base of the cantilever is raised or lowered to ensure that the cantilever deflection remains constant. If the deflection becomes too low

or too high, the cantilever is moved closer to or further from the sample, respectively. By considering Hooke's Law,

$$F_{ts} = k * \delta \tag{1}$$

where F_{ts} is the tip-sample interaction force, k is the cantilever force constant, and δ is the tip deflection, it is clear that if a setpoint deflection ($\delta_{setpoint}$) is maintained, the tip-sample interaction force will remain constant. The prescribed setpoint deflection is set by the user and can be increased or decreased to vary the amount of force exerted on the sample. The cantilever base height required to maintain the setpoint deflection is used as the height trace of the sample and this information is transferred to the computer to construct the three-dimensional image.

There are some intrinsic disadvantages to imaging in contact mode since the setpoint force necessary to obtain quality images can range from nanonewtons to micronewtons. The higher the force, the better the AFM is able to image deep trenches and other features. However, these high repulsive forces are capable of permanently damaging soft samples. Since the probe is dragged along the sample, lateral friction forces are also present. If the tip is pressed hard on the sample, the resultant lateral forces will also increase, which can permanently damage the sample through tearing. Therefore, soft samples are difficult to image in contact mode.

2.2.2   Amplitude Modulation

An entirely new set of AFM capabilities emerged with the implementation of Amplitude Modulation Atomic Force Microscopy (AM-AFM) [21].   AM-AFM is considered the first dynamic AFM mode because the cantilever tip oscillates above the

sample. More details on the dynamics of an oscillating cantilever when subjected to a forced harmonic excitation and molecular interaction forces can be found in Section 2.4 and the references provided therein. However, a qualitative explanation of the tip dynamics is necessary for an understanding of the AM-AFM operation. The cantilever is excited at or around its free resonance frequency with a free amplitude determined by the user. As the cantilever is lowered toward the sample, the effective cantilever force constant is altered. This change in the cantilever stiffness is due to the gradient of the tip-sample interaction forces causing the cantilever to act stiffer or softer depending on whether repulsive or attractive forces are dominating. A change in the effective k causes a change in the effective resonance frequency. The offset between the excitation frequency and effective resonance frequency causes the amplitude of oscillation to decrease. The cantilever base continues to be lowered toward the sample until the amplitude has reached the prescribed setpoint amplitude, which must be less than the free oscillation amplitude. The AFM then scans laterally across the sample, increasing or decreasing the base height to maintain the setpoint amplitude. Throughout this process, the excitation force is maintained to have a constant drive amplitude and constant frequency. The height required to maintain the setpoint amplitude is used as the height trace of the sample and this information is fed into the computer to construct the three-dimensional image, as done in contact mode.

Similar to contact mode, there are a number of limitations and consequences associated with operating in AM-AFM mode. Although AM-AFM has been shown to work in a non-contact mode [22], where the tip does not come in mechanical contact with the sample, it is usually referred to as tapping mode AFM. Due to the relatively large

amplitudes required in AM-AFM, the probe often penetrates deep into the sample resulting in high repulsive forces. These high forces can cause permanent sample damage as seen in contact mode. Another issue with AM-AFM is bistability. As a result of the nonlinear characteristics of the tip-sample interaction forces, two stable oscillation states exist with two different amplitude values [23-25]. For a given set of external parameters (cantilever equilibrium position $\{Z_{eq}\}$, resonance frequency $\{\omega_o\}$, and drive force $\{F_o\}$), the initial conditions determine whether the cantilever vibrates in the low amplitude branch or high amplitude branch [26]. In Figure 2.2, a representative example of how two amplitudes of oscillation can exist for a given cantilever base equilibrium height is provided. During imaging, it is possible to see jumps between the low and high amplitude branches, which cause image distortion. Also, there is potential for sample damage to occur due to the increase in repulsive forces experienced when oscillating in the high amplitude branch.
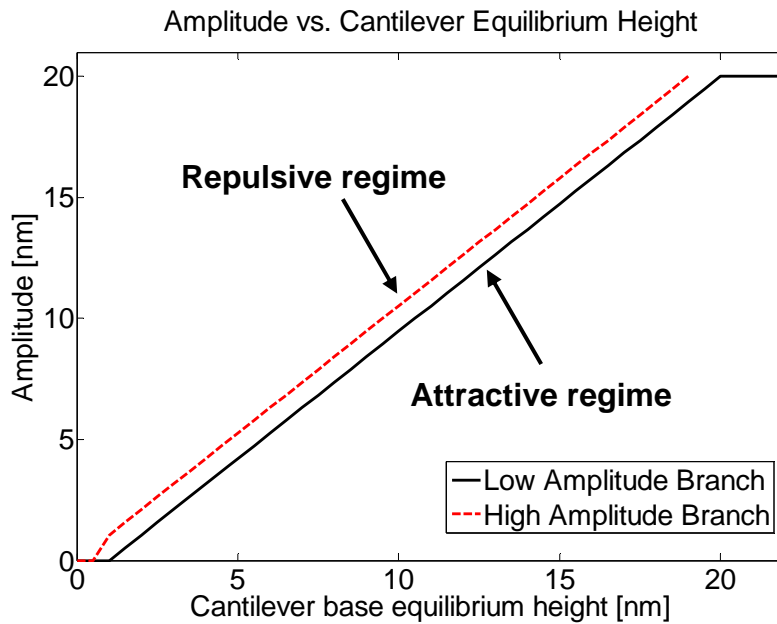
Figure 2.2 – Representative graph showing bistability

7

2.2.3 Frequency Modulation

In 1991, another substantial development in dynamic AFM occurred with the development of Frequency Modulation Atomic Force Microscopy (FM-AFM) [27]. Albrecht *et al.* discovered a way to utilize the high sensitivity measurements achieved through increasing the quality factor (Q) of the oscillating cantilever. The AM-AFM mode of operation was incapable of taking advantage of the higher sensitivity associated with higher quality factors due to the resultant drop in bandwidth. The drop in maximum available bandwidth is attributed to the linear increase in response time (τ) with increasing Q

$$\tau = \frac{2*Q}{\omega_o} \tag{2}$$

Albrecht *et al.* proposed a mode in which the frequency is modulated rather than the amplitude. As seen in AM-AFM, changes in the force gradient result in changes to the effective frequency of oscillation. The control scheme is designed so that the amplitude remains constant while the phase and frequency of excitation are adjusted. As a result, the frequency of oscillation remains at a prescribed offset from the free resonance frequency and the excitation leads the response by 90 degrees, ensuring maximum positive feedback. The base of the cantilever is raised or lowered throughout the scan to ensure the frequency offset setpoint is maintained. In a procedure similar to the other modes of operation, the height required to maintain the setpoint frequency offset is used as the height trace of the sample and this information is transferred to the computer to construct the three-dimensional image.

As with the other modes, FM-AFM has its own set of intrinsic limitations. FM-AFM is often referred to as Non-Contact (NC) mode because the cantilever usually

vibrates with an amplitude that is small enough to prevent mechanical contact. These small amplitudes have negative consequences when imaging. Since the probe does not reach the sample, the true sample skin cannot be determined. This can lead to a tip broadening effect where the features of a sample appear wider than they actually are. An illustration of the effect of tip broadening is shown in Figure 2.3. Another possible consequence of using FM-AFM is that the small amplitudes of oscillation make it difficult to accurately image samples with drastic changes in topography.
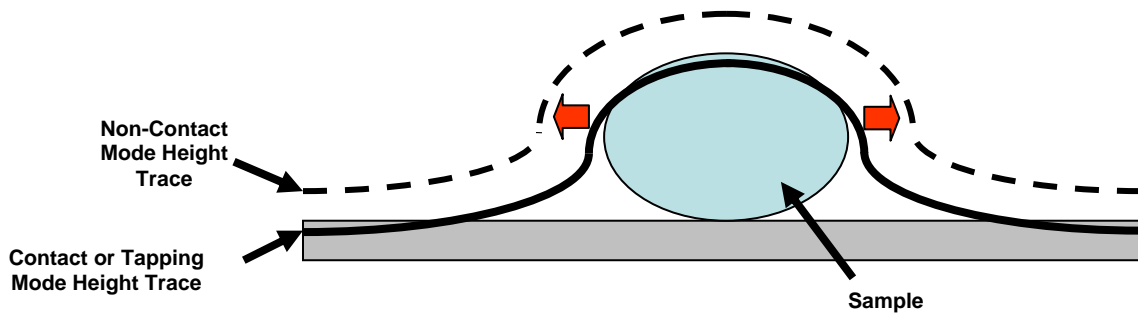
Figure 2.3 - Tip broadening effect experienced during non-contact imaging

2.3   *Tip-Sample Interaction Forces*

As the tip moves relative to the sample, it experiences varying forces. These forces include, but are not limited to, van der Waals forces, mechanical contact forces, chemical bonding, electrostatic forces, and capillary forces. The tip-sample interaction forces depend on the geometry and material of the tip, as well the material and chemical composition of the sample. External factors such as electric fields and water layers also play a role in determining the forces between the tip and the sample. As previously indicated, these interaction forces affect the deflection of the cantilever in

contact mode or the amplitude, effective resonance frequency, and phase of the oscillation in dynamic modes.

A wide range of models are necessary to account for the different components of the complete tip-sample interaction forces. Assuming these forces can be derived from a potential function, a simple model used to represent both the attractive and repulsive interaction forces between molecules is the Lennard-Jones Potential

$$V(r) = 4\varepsilon \left(\frac{\sigma^{12}}{r^{12}} - \frac{\sigma^{6}}{r^{6}} \right)$$

(3)

where V is the potential energy between molecules, r is the distance between molecules, ε is the depth of the potential well, and σ is the location of zero potential energy. The force between two molecules under the Lennard-Jones model is found by calculating the negative gradient of the potential. Since the tip-sample interaction forces are essentially the forces between many different molecules, a Lennard-Jones model is one way to represent the interaction forces.

Numerous other models exist which characterize the interaction forces between the tip and the sample for the sphere-flat geometry approximation. The sphere-flat geometry assumes that the end of the tip is spherical in shape and that the sample is flat over the contact area. These assumptions usually hold true as many probes are designed to have spherical ends with a radius of curvature on the order of tens to hundreds of nanometers. The small radius of curvature results in a reduced contact area between tip and sample. Topographical changes over the small contact region are unlikely to be significant; therefore, the sample can usually be modeled as a flat plate. Under the

sphere-flat geometry approximation, the long-range attractive forces, due to van der Waals forces, are most often modeled as

$$F(Z) = -\frac{H*R}{6*Z^2}$$ (4)

where F is the interaction force, Z is the tip-sample separation, H is the Hamaker constant, and R is the radius of the curvature of the tip [23]. As mentioned, other effects can factor into the long range forces; however, this model only accounts for long range attractive forces due to Van der Waal forces.

While the above equation is well accepted for modeling long range forces, multiple models are used to capture the contact mechanics under the sphere-flat approximation. A commonly used contact model was developed by Derjagiun, Muller, and Toporov, referred to as the DMT model [28]. The DMT model represents the contact mechanics of rigid systems with small radii of curvature and small adhesion forces. Like the Hertzian contact model, DMT does not account for any deformation of the contact geometry or for hysteresis between the loading and unloading adhesion forces. However, in contrast to the Hertzian model, the DMT model does account for surface forces outside the contact area [29]. In DMT, the long range attractive forces are modeled by using equation (4), which are dominant when the tip-sample separation is greater than the interatomic equilibrium distance (a_o). When the tip-sample separation is less than the interatomic equilibrium distance, the forces are modeled with

$$F(Z) = -\frac{H*R}{6*a_o^2} + \frac{4}{3}E^* * \sqrt{R} * (a_o - Z)^{3/2}$$ (5)

where E^* is equal to

$$\frac{1}{E^*} = \frac{1-\nu_t}{E_t} + \frac{1-\nu_s}{E_s} \tag{6}$$

where E_t and E_s are the elastic moduli of the tip and sample, respectively, and ν_t and ν_s are the Poisson ratios for the tip and sample, respectively [30]. Additional models of increasing complexity that account for more factors include those due to: Burnham, Colton and Pollock (BCP) [31]; Johnson, Kendall, Roberts, Sperling (JKRS) [32]; Maugis [33]; and others. Each model contains a different set of assumptions and simplifications [29].

2.4 *AFM Dynamics*

A thorough comprehension of the dynamics of the AFM cantilever is vital to understanding dynamic AFM modes for both experimental and computer modeling applications. A brief overview of AFM dynamics is provided below and more details can be found in various references, including [26, 30, 34-39]. The standard governing equation for the vibration of a one-dimensional beam under external loading is

$$EI\frac{\partial^4 w(x,t)}{\partial x^4} + \mu\frac{\partial^2 w(x,t)}{\partial t^2} = F(x,t) \tag{7}$$

where w is the displacement field of the beam, x is the location along the beam, t is time, E is the Young's modulus, I is the moment of inertia, µ is the mass per unit length of the beam, and F is the external force field acting on the beam. The boundary conditions for this system are that of a cantilever beam, supported on one end and free on the other end. Due to the non-linear characteristics of the external load (as a result of non-linear tip-sample interaction forces) and the fact that the equation is a fourth order partial

differential equation, a numerical solution to this equation for a given set of imaging conditions is difficult to obtain. However, in most dynamic mode AFM operations, only the first eigenmode of the cantilever is excited and the AFM tip motion is the focus. Therefore, it is a common practice in dynamic modeling of AFMs to consider the motion of the tip as that of a point-mass spring system with damping [15, 26, 38, 39]. The motion of the tip can then be modeled as

$$m\frac{d^2Z(t)}{dt^2}+\frac{m\omega_o}{Q}\frac{dZ(t)}{dt}+k*[Z_{eq}-Z(t)]=F_{ts}+F_o\cos(\omega t) \tag{8}$$

where Z is the tip position relative to the sample, Z_{eq} is the cantilever rest height, F_{ts} is the tip-sample interaction force, F_o is the excitation force, and ω is the frequency of excitation. This equation is a second order ordinary differential equation, which is less complex and can be solved through numerical integration.

To further investigate the dynamics of the tip, much work has been conducted in assuming the tip motion resembles that of a forced harmonic oscillator with damping and by using perturbation theory. In the absence of tip-sample interaction forces (F_{ts}), equation (8) is the same as that governing a forced harmonic oscillator. Therefore, as long as the interaction forces are small compared to the excitation force and restoring force, a forced harmonic approximation is appropriate.

As briefly discussed in the explanation of AM-AFM operation, the frequency of oscillation changes as the tip approaches and then makes contact with the sample. The correlation between the instantaneous, or effective, resonance frequency and the gradient of the tip-sample interaction forces is

$$\omega_{eff} = \sqrt{\frac{K - \dfrac{dF_{ts}}{dZ}}{m}} \qquad (9)$$

where ω_{eff} is the effective angular frequency of oscillation, Z is the distance between the probe and sample, and m is the effective mass. Unless the frequency of excitation is altered to match the new effective resonance frequency, as done in frequency modulation modes, the difference between the excitation and effective resonance frequencies will cause the amplitude of oscillation to decrease. Under the forced harmonic oscillator assumption, the dependence of the amplitude on the two frequencies is

$$A(\omega) = \frac{F_o / m}{\sqrt{\left(\omega_{eff} - \omega\right)^2 + \left(\omega * \omega_{eff} / Q\right)^2}} \qquad (10)$$

where $A(\omega)$ is the amplitude at the excitation angular frequency. The phase also shifts as the effective resonance frequency changes by

$$\tan(\phi) = \frac{\omega * \omega_{eff} / Q}{\omega_{eff}^2 - \omega^2} \qquad (11)$$

where ϕ is the phase shift expressing how the tip response lags behind the excitation. By examining equations (9) and (11), it can be observed that when the tip is in the attractive regime, the effective resonance frequency is lower than the free resonance frequency and the phase shift is greater than 90 degrees. When the tip experiences a sufficient repulsive force to cause the force gradient to be positive, the frequency shift is positive and the phase shift is less than 90 degrees.

In FM-AFM, the excitation frequency is maintained at the effective resonance frequency, which equations (10) and (11) show that the amplitude remains constant and the phase remains at 90 degrees. An important concept for understanding FM-AFM

14

dynamics is the relationship between the frequency shift ($\Delta\omega = \omega_{eff} - \omega_o$) and the tip-sample interaction forces, which has been extensively explored [1-6, 26, 34, 40]. A common method of relating the frequency shift and tip-sample interaction forces is through the use of perturbation theory, first used by Giessibl [1]. Since then, many others have continued this work [2-5] by applying a variety of perturbation schemes. The general result to this work is the correlation

$$\Delta f = -\frac{1}{2\pi} \frac{f_o}{K * A_o} \int_0^{2\pi} F_{ts}[Z_{eq} + A_o \cos(\varphi)] * \cos(\varphi) d\varphi \qquad (12)$$

where $f_o = \frac{\omega_o}{2\pi}$ and A_o is the amplitude of oscillation ($A_o = \frac{Q * F_o}{k}$). Equation (12) is based on perturbation theory, which requires the same conditions as those for the forced harmonic oscillator approximation. It is assumed that the cantilever restoring force is significantly greater than the tip-sample interaction forces, which are on the order of nanonewtons. This ensures the motion of the cantilever remains approximately harmonic. The implications of equation (12) and the assumptions made to formulate it are discussed in the following setup and results sections.

2.5   *Frequency and Force Modulation Atomic Force Microscopy*

2.5.1   Motivation

While the main AFM modes of operation described above have been proven over the years to adequately perform a great number of tasks, many of the limitations associated with these methods pose problems when imaging or characterizing certain types of samples. One such area is the use of AFM on soft samples, including many

biological samples. These soft samples are often times permanently damaged in AM-AFM or Contact modes due to the high lateral and normal forces. Bistability also causes distortion which leads to inaccurate images. While FM-AFM may solve both these issues, a non-contact mode generally does not produce accurate images of the true sample skin or samples with drastic topographical changes. To accurately scan soft biological samples, Solares has developed a new mode of AFM in which the frequency is modulated to prevent bistability and the force is modulated to minimize sample deformation [41-44]. This new mode of operation, Frequency and Force Modulation – Atomic Force Microscopy (FFM-AFM), operates in tapping mode, which allows for more accurate scans, see Figure 2.3. It has since been revealed that FFM-AFM may have applications in the mechanical characterization of more than just biological samples, expanding the potential applications of FFM-AFM.

2.5.2   FFM Operation and Controls

In FFM-AFM, the cantilever base is maintained at a constant height throughout the scan. This height is determined by the user depending on an estimation of the maximum changes in sample height throughout the scan size. As experimental implementation of FFM-AFM has begun, multiple methods have been developed to determine the height the cantilever base maintains as it scans. One such method is to incorporate the controls of Asylum Research's Simplified NAP mode (SNAP). NAP mode is similar to a mode of operation referred to as "lift mode," which has been used for a variety of applications in AFM [45-47]. In SNAP mode, the AFM makes the first pass along the surface of the sample in AM or contact mode, and then determines a linear fit to

the height trace. Then the cantilever scans the next line with the base of the cantilever fixed to the linear line determined by the first pass, only with a prescribed delta height offset. SNAP mode can be modified to use the FFM control scheme during the second pass. Another potential method of determining the cantilever base height is to determine the height of the sample at the four corners of the scan area and fit a plane to those height values. The plane will then determine the height of the cantilever base throughout the scan area. This method could prove problematic if the four corners of the scan size have extremely low heights compared to an object in the middle of the scan size. However, the response time is not affected by the amplitude and it will be shown in Section 4 that large equilibrium heights do not affect sample deformation. Therefore, conservative estimates of the delta height can be made to ensure clearance without reducing the quality of an image.

After determining the height of the cantilever base throughout the scan, the FFM controls must be incorporated. As in FM-AFM, FFM-AFM must maintain a 90 degree phase offset between the excitation force and the cantilever response in addition to an excitation frequency equal to the instantaneous effective resonance frequency. Unlike FM, where the height of the cantilever is changed to maintain a desired frequency shift, in FFM the drive amplitude is controlled to increase or decrease the amplitude of oscillation. This change in amplitude is used to maintain the desired frequency offset. The height of the sample is then determined by the difference between the height of the cantilever base and the amplitude of oscillation. A diagram of the control scheme used for FFM is shown in Figure 2.4.

Measure free resonance frequency, f_o
Input frequency setpoint, f_{set}
Input cantilever equilibrium height, Z_{eq}
Position cantilever at Z_{eq}
Set excitation force to $F_o\cos[(2\pi f_o)t]$
with $F_o=Z_{eq}k/Q$
Begin imaging

Continuously update the excitation force frequency and amplitude:
$F_o\cos[(2\pi f)t-\varphi+90^o]$

Continuously record the sample height: $Z_{eq}-A$

Fit tip position signal to:
$Z(t)=A_o\cos[(2\pi f)t-\varphi]$
A_o = Amplitude
f = Frequency
φ = Phase

Increase F_o

Decrease F_o

Compare
f to f_{set}

$f < f_{set}$

$f > f_{set}$

Figure 2.4 - FFM-AFM control scheme

3   Setup and Procedures

3.1   *Introduction*

The focus of this investigation was to determine how each imaging parameter affected the tip penetration into the sample during imaging, and consequently the maximum repulsive force exerted on the sample, using the FFM-AFM control scheme. Since FFM-AFM is still in developmental stages and a fully functioning FFM-AFM has not yet been implemented, all results were gathered through the use of simulations. As previously mentioned, the integration of equation (6) has proven reliable in simulating AFM results. Consequently, each variable included in the equation of motion was considered as a parameter potentially affecting the maximum tip penetration. The list of all parameters consisted of m, $Z_{eq,}$ ω_o, Q, k, F_o, ω, and any parameters used to describe the tip-sample interaction forces (F_{ts}).

3.2   *Modeling of Interaction Forces*

The tip-sample interaction forces are the driving factors affecting changes to the AFM cantilever motion during imaging. With many different types of tip-sample interaction force models in use, it was important to find a model that fit the needs of the work being conducted. Since the impact on each parameter seen in the equation of motion required investigation, it was vital to determine a force model that limited the number of variables. For each new parameter introduced into the investigation, the total number of simulations required to fully understand each parameter's effect would

19

increase exponentially. With models such as the DMT model containing four variables

(H, R, a_o, and E^*), the true purpose of the study would become lost in the complexity of

the parameter space and the hundreds of thousands of simulations.

A model previously developed by Solares has only two dependent parameters,

maximum attractive force (W) and repulsive force steepness (S) [43, 44]. The

formulation of this model began with molecular dynamics simulations of various silicon

and carbon nanotube tips approaching different sample materials. As the tips were

lowered toward the sample, the potential energy of the system at each stage was recorded.

The forces were then determined by the negative of the potential gradient. A detailed

description of this method can be found in reference [48]. The data was then shifted so

that the maximum attractive force occurred at Z=0. Therefore, positive Z values

represented a separation between the tip and sample and negative Z values indicated

penetration into the sample. As seen in many interaction force models, two separate

equations were used to model the attractive (Z > 0) and repulsive (Z < 0) forces

individually. The attractive force equation was selected to only depend on $1/Z^2$ and the

maximum attractive force W. This yielded an equation similar to the long-range force

model for the sphere-flat approximation. The repulsive force equation used W, S, and Z^2

as dependent terms. After finding models that best captured the molecular dynamics

results, the following equations were determined

$$F_{ts} = \frac{-W}{1+30*Z^2} \quad for\ Z \geq 0$$
$$F_{ts} = -W + S*Z^2 \quad for\ Z \leq 0$$

(13)

In Figure 3.1, atomistic models used in the molecular dynamics simulations are shown for three of the tip-sample combinations used. The results to these simulations are displayed as graphs in Figure 3.2. The data used to construct the graphs were first reported in references [44] and [49]. The three cases shown are: (a) a 15 nm radius silicon tip approaching a Si(100)-OH surface, (b) a 5.4 nm radius single-walled carbon nanotube tip approaching a Si(100)-OH surface, and (c) a 2.4 nm radius triple-walled carbon nanotube approaching a bacteriorhopdpsin molecule.
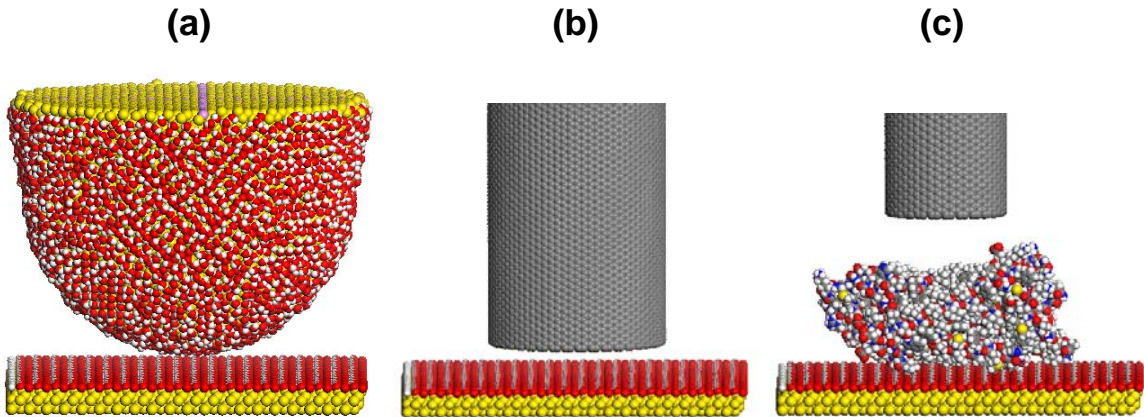
Figure 3.1 - Atomistic models used in the molecular dynamics simulations for the three cases described above [40, 57].
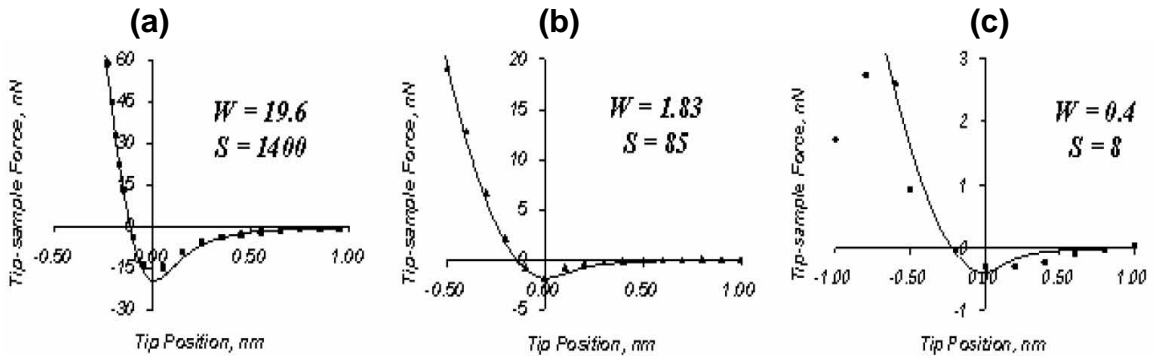
Figure 3.2- Tip-sample interaction forces for the three cases described above. The square markers represent the molecular dynamics data and the solid lines show how closely equation (13) matches the data for the corresponding values of W and S [40, 57].

It is important to note that throughout this investigation the term penetration refers to a negative tip-sample separation in the above model. Physically, this implies that the tip is closer to the sample than the interatomic spacing, the point at which the maximum attractive force occurs. It is therefore possible to have a tip penetration, but a net interaction force that is still attractive.

3.3   *Determination of Final Parameters and Ranges*

With a tip-sample interaction force model now determined, the equation of motion of the AFM tip is

$$m\frac{d^2 Z(t)}{dt^2} + \frac{m\omega_o}{Q}\frac{dZ(t)}{dt} + k*(Z(t) - Z_{eq}) = F_{ts}(W, S, Z(t)) + F_o \cos(\omega t) \qquad (14)$$

To reduce the number of simulations and decrease the complexity of the problem, many variables included in the equation of motion were eliminated from the final investigation. First, the resonance angular frequency can be related to cantilever force constant by the relation

$$\omega_o = 2\pi * \alpha * k \qquad (15)$$

when operating in air ($50 \leq Q \leq 1000$). While cantilevers can be manufactured with α ranging from 10^3 to 10^5, an examination of many cantilevers on the market showed that most cantilevers have an α value of approximately 10^4. Preliminary simulations suggested the resultant tip penetration had little to no dependence on α. It has been observed that the resonance frequency is reduced by a factor of three when operating in a liquid ($1 \leq Q \leq 10$) [26]. Therefore, a final relation between ω_o and k is

$$\omega_o = 20,000\pi * k \qquad 50 \leq Q \leq 1000$$
$$\omega_o = \frac{20,000\pi * k}{3} \qquad 1 \leq Q \leq 10 \tag{16}$$

The angular frequency of harmonic oscillators can also be calculated by the relationship,

$\omega_o = \sqrt{\dfrac{k}{m}}$. When combined with equations (16), the mass can be determined through

$$m = \frac{1}{(20,000\pi)^2 * k} \qquad 50 \leq Q \leq 1000$$
$$m = \frac{9}{(20,000\pi)^2 * k} \qquad 1 \leq Q \leq 10 \tag{17}$$

The other parameters that can be eliminated from the investigation are the excitation force parameters. As previously described, the excitation amplitude is varied to achieve a desired effective resonance frequency and the frequency of excitation is kept equal to the effective resonance frequency. Therefore, both F_o and ω are determined by the feedback loop and cannot be externally controlled. Therefore, five parameters remain which can be controlled during a zero frequency shift FFM-AFM operation, including the following: the cantilever rest height, Z_{eq}; the cantilever force constant, k; the quality factor, Q; the maximum tip-sample attractive force, W; and the steepness of the tip-sample repulsive force region, S.

An appropriate range for each parameter was determined to best represent the imaging conditions most likely to be used when operating in FFM-AFM. The cantilever rest height was varied between 15 nm and 125 nm. This would account for topographical changes of up to 115 nm. Given the potential for long response times under certain conditions, FFM will initially be used on relatively flat samples. While improved gains, controls, and conditions may decrease the response time in the future, changes in surface

height of no more than 115 nm will be accounted for at this time. The cantilever force constant values were determined by examining the current dynamic mode cantilevers on the market. Despite a few exceptions, nearly all cantilevers contained force constants between 1 N/m and 50 N/m. Use of force constants below 1 N/m would require large amplitudes to ensure that the restoration force greatly exceeds the maximum attractive force. It would also require longer equilibration times as the low frequency values cause long response times. Force constants higher than 50 N/m also seemed unnecessary as few cantilevers in production have higher values and none of the foreseeable applications of FFM require a force constant higher than 50 N/m. As with all of these parameters, if the need arises for imaging conditions outside the specified ranges, the methods used here can be applied to new imaging conditions. When imaging in both liquid and air, the quality factor values are known to range from 1 to 10 and 50 to 1000, respectively [26]. Knowledge gained from previous molecular dynamics simulations of varying tip-sample combinations suggested that an appropriate range of maximum attractive force values was from 0.5 to 50 nN. It was also determined that repulsive regime steepness values between 5 and 1500 nN/nm^2 would be adequate to model most tip-sample interaction forces experienced during AFM operation.

3.4 *Imaging Parameter Combinations*

The five independent imaging parameters led to a high number of imaging condition combinations. With runtimes of each simulation varying from a few minutes to several hours, the process of determining the sample deformation and tip-sample interaction forces for all conditions would be too computationally expensive to perform.

For example, using five different values per parameter yields 3125 combinations, which would require over 130 days of computation time, assuming a conservative estimate of one hour per simulation. This estimate also fails to address the need of running certain simulations with multiple simulation parameters to determine optimal values and account for inaccurate results due to incorrect simulation parameters. A reasonable compromise between thoroughness and efficiency was to select the lowest, highest and one intermediate value for each parameter. A summary of the parameters used for the investigation and the ranges studied is contained in Table 3.1. Following the examination of all 486 possible combinations from these parameter values, further simulations were run for various intermediate values. Note that the units of these parameters indicated in Table 3.1 are used throughout this thesis.

Parameter	Symbol	Low Value	Middle Value	High Value	Units
Cantilever equilibrium height	Zeq	15	55	125	nm
Cantilever force constant	K	1	25	50	N/m
Quality factor (Air)	Q	50	500	1000	-
Quality factor (Liquid)		1	5	10	-
Max attractive force	W	0.5	25	50	nN
Steepness of repulsive regime	S	5	7500	1500	nN/nm^2

Table 3.1 - Imaging parameter ranges used during investigation

3.5   *Analytical Method*

3.5.1   Simplification of Frequency Shift Equation

As mentioned in the AFM dynamics section, one of the most accepted ways to relate the tip-sample interaction forces to the shift in effective resonance frequency is through equation (12). For the simulations performed in this thesis, the effective resonance frequency is maintained at the free oscillation resonance frequency, resulting

in a frequency shift of zero. The most important observation on equation (12) related to this investigation is that many of the imaging parameters can be ignored when the frequency shift is set to zero. Since f_o, k, and A_o are all nonzero values, the integral term must be zero. Therefore, equation (12) can be simplified to

$$0 = \int_0^{2\pi} F_{ts}[Z_{eq} + A_o \cos(\varphi)]\cos(\varphi)d\varphi \qquad (18)$$

This suggests that when operated for a zero frequency shift, the only parameters affecting the tip penetration are those defining the interaction forces (W and S) and the rest position (Z_{eq}). Consequently, neither the force constant nor the quality factor appear to have any impact on tip penetration or sample damage.

3.5.2 Numerical Integration of Frequency Shift Equation

In order to compare the simulation results to the theoretical frequency shift equation, it was necessary to solve the integral in equation (18) for the penetration. Since every term is known except A_o, the equation can be solved to determine the amplitude of oscillation required to attain a zero value for the integral. This process was performed through numerical integration using a built-in MATLAB function, quadl, which utilizes recursive adaptive Lobatto quadrature. After assuming an initial amplitude equal to the cantilever rest position, the amplitude was incrementally changed until the integral term equaled zero. The penetration into the sample (ρ) was defined as $\rho = A_o - Z_{eq}$.

3.6   Simulation Method

To simulate how the AFM will operate under a given set of imaging parameters, a method to solve the second order nonlinear ordinary differential equation of motion was required. Utilizing the Verlet algorithm [50], numerical integration was conducted to solve for the position and velocity of the tip at a given increment of time. Acceleration was calculated through the equation of motion with initial conditions Z(t=0) and V(t=0) set to zero when calculating a(t=0). The Verlet algorithms for acceleration, position, and velocity are

$$a(t) = \frac{-k*(Z(t) - Z_{eq}) - \dfrac{m*\omega_o*V(t)}{Q} + F_{ts}(W, S, Z(t)) + F_o*\cos(\omega*t)}{m} \tag{19}$$

$$Z(t + \Delta t) = 2*Z(t) - Z(t - \Delta t) + a(t)*\Delta t^2 \tag{20}$$

$$V(t + \Delta t) = \frac{Z(t + \Delta t) - Z(t - \Delta t)}{2*\Delta t} \tag{21}$$

where Δt is the timestep of integration.

The simulations were run in a manner in which the cantilever initially vibrated without any control loops modulating the frequency, amplitude, or force. This process ensured that the cantilever made contact with the sample before modulation began. In earlier results, the tip never made contact with the sample when adequate equilibration time was not provided. One such case is shown in Figure 3.3.

AFM Tip Trajectory without Equilibration Time

(Zeq=125, K=50, Q=1, W=0.5, S=5)
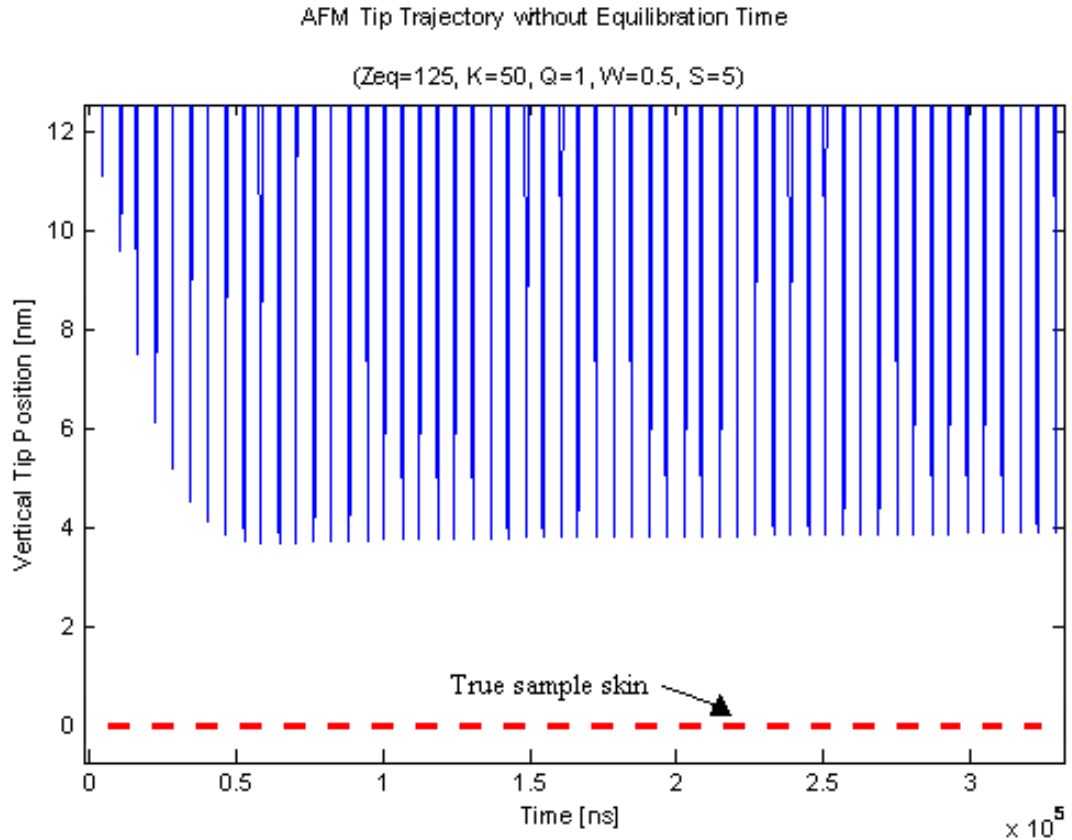
Figure 3.3 - Tip trajectory showing sample skin is never reached when adequate equilibration time is not provided

After equilibration, the FFM-AFM control scheme was activated to maintain a phase shift of 90 degrees and a frequency shift of zero hertz. The phase was maintained by introducing a separate time term (t_{ext}) into the excitation force. Setting the excitation time to zero at the beginning of each oscillation enabled the excitation force to be greatest when the tip was at the cantilever equilibrium height. A PID controller was used to adjust the excitation force, which consequently adjusted the amplitude of oscillation. This served as the main feedback loop in FFM, which modulated the frequency by varying the amplitude. The gains for the PID controller required fine-tuning depending on the imaging parameters to ensure the rise time, overshoot, and steady state error were

all at acceptable values. Further discussion on how the timestep, simulation length and PID gains where varied for each set of conditions are discussed in the following section.

After providing adequate time for the control loop to achieve the correct amplitude resulting in a zero frequency shift, the minimum point reached by the tip over the last 10 oscillations was recorded. This point was defined as the maximum tip penetration for zero frequency shift, steady-state oscillations for the specified imaging conditions. The maximum repulsive force experienced at that point was found by evaluating the tip-sample interaction force model at the penetration point.

3.7   *Adjustment of Simulation Parameters*

The wide range of imaging parameters caused nearly all aspects of the simulation to vary from one set of conditions to another. Therefore, one set of simulations parameters could not be used to produce accurate results and minimize computation time. The simulation parameters which required condition-specific values were the timestep of integration, length of simulation, and the PID gains.

Significant changes in tip speed caused the need for variations in the timestep of integration. For example, a 1 N/m cantilever oscillating in liquid with an amplitude of 15 nm would have an average speed of 200,000 nm/s. However, a 50 N/m cantilever oscillating in air with an amplitude of 125 nm would have an average speed of 25,000,000 nm/s. With an average speed 125 times greater under the second set of imaging conditions, an integration timestep that was consistent, efficient, and accurate in all cases could not be achieved. To address the need for varying timesteps, a simple

relation between the timestep, frequency of oscillation, and amplitude of oscillation was required. The number of integration points per oscillation (NPPO) is calculated by

$$NPPO = \frac{1}{f * \Delta t} \qquad (22)$$

where Δt is in seconds and f is in Hz. Since the tip velocity increases as the amplitude increases, the timestep should be inversely proportional to the equilibrium height. The final equation to determine an appropriate timestep of integration is

$$\Delta t = \frac{1}{f * NPPO * Z_{eq}} \qquad (23)$$

Through trial and error, an adequate value for NPPO was set at 500. Timesteps smaller than that calculated through equation (23) were found to have little to no effect on the accuracy of the results.

The length of time in which the integration occurred also depended on the imaging conditions. The required length of the simulation depended on the length of the two phases during the simulation. The first phase was the period of time required for the tip to reach full amplitude before FFM controls were activated (time for tip to first reach the sample), which was dependent on the quality factor and the resonance frequency. The time needed for the amplitude to reach e^{-1}, or 36.79%, of the steady state amplitude is:

$$\tau = \frac{Q}{\pi * f_o} \qquad (24)$$

To find the time required to achieve 99% of the steady state amplitude (meaning the transient term is reduced by 99%), the following calculations are performed.

$$\tau_{0.99} = \frac{\beta * Q}{\pi * f_o}, \quad where \quad \beta = \frac{\ln(1-0.99)}{\ln(1/e)} = \frac{\ln(0.01)}{-1} \tag{25}$$

Therefore,

$$\tau_{0.99} = \frac{-\ln(0.01) * Q}{\pi * f_o} \tag{26}$$

The second phase of the simulation, where the PID controls attempt to modulate the frequency by changing the excitation force, is dependent both on the response time of the system and the PID gains used. This phase could also be defined as the time required to reach a steady-state oscillation with a zero frequency shift. The quicker the response time, the faster the system responded to the change in excitation force while trying to achieve a zero frequency shift. When higher gain values were used, the change in excitation force after each oscillation was more drastic. Therefore, less time was required to achieve the necessary zero frequency shift. Due to many influencing factors, a consistent expression for the time required to reach a zero frequency shift was difficult to obtain. A general guideline of ten times $\tau_{0.99}$ proved to be adequate time for most conditions and average gain values.

As mentioned above, the PID gains were a significant determinant for the required simulation length. With run-times reaching a few hours in many cases and hundreds of imaging condition combinations to run, it was necessary to use the highest PID gains possible. The initial set of gains were -0.005 nN/kHz, -0.0003 nN/kHz, and -0.65 nN/kHz for the proportional gain, integral gain, and derivative gain, respectively. These gains were determined to be the optimal values for the widest range of imaging

conditions. However, the interaction force gradient has a more significant effect on the effective frequency when large tip-sample interaction forces are present. Therefore, high PID gains may cause the excitation force to change too drastically from one oscillation to the next, causing a steady-state error as shown in Figure 3.4.
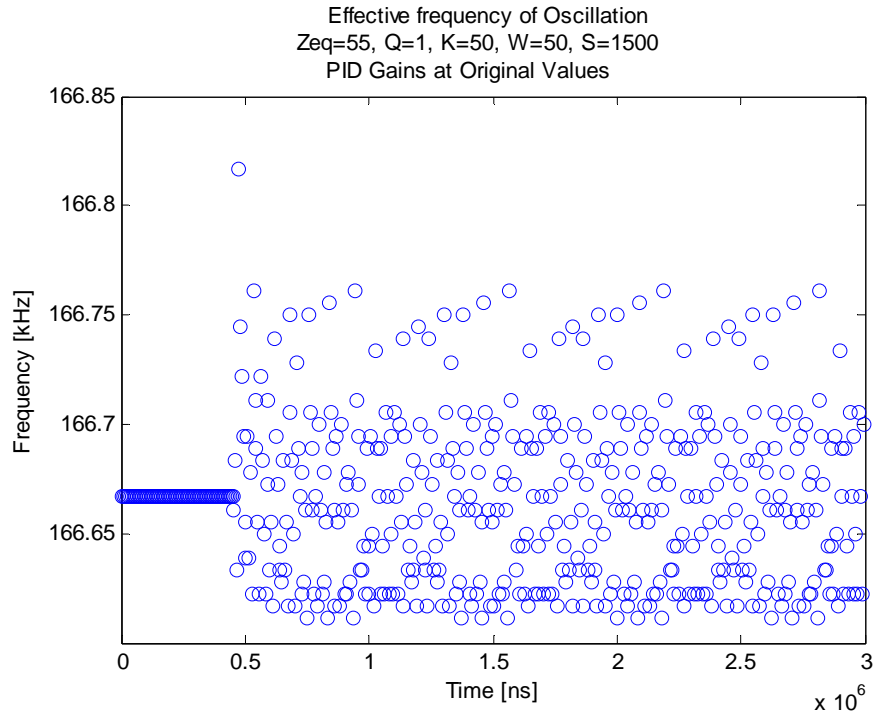
Figure 3.4 - Instability in tip motion due to high PID gains

In Figure 3.4, sporadic frequency values up to 100 Hz above resonance are shown. This led to penetration values over 50% higher than the theoretical values. In Figure 3.5, it is demonstrated as to how reducing the PID gains by 50% eliminated the errors and produced a penetration value in agreement with the theoretical result.
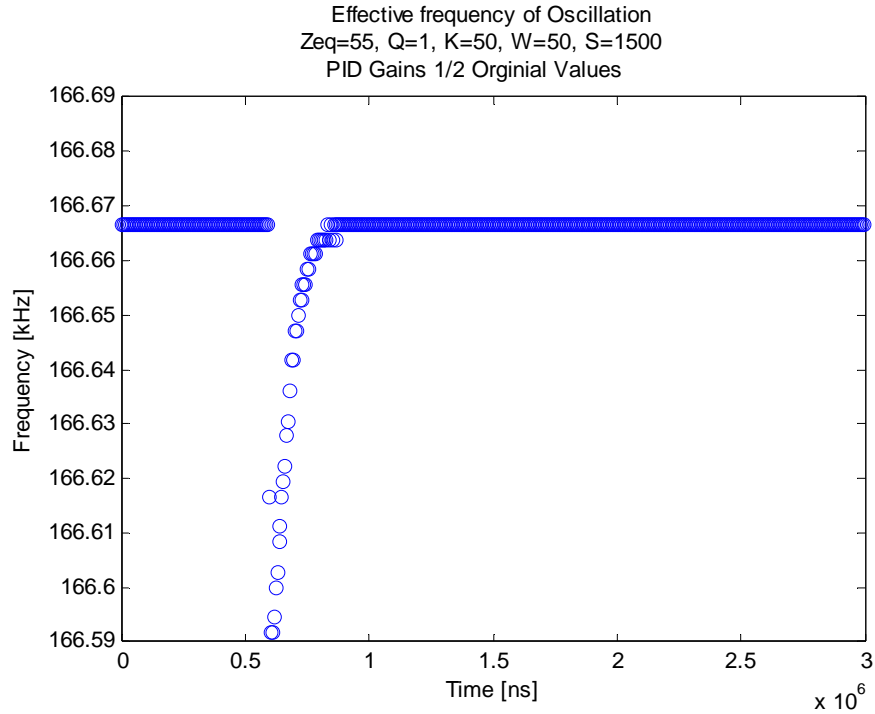
Figure 3.5 - Stable tip oscillations due to lower PID gains

This phenomenon was most likely to occur for lower quality factors where the fast response time allows for the changes in excitation force to take effect faster. It was initially expected that the instability due to high PID gains would only occur with low force constants where small changes in the interaction force cause large changes in the effective resonance frequency. However, from Figure 3.4 and Figure 3.5, one learns that high force constants also experienced instability due to aggressive gains under certain conditions. The PID gains were changed from the initial values on a case by case basis when the simulation results did not match the theoretical results from equation (18).

4 Results and Analysis

4.1 *Theoretical Results of Frequency Shift Equation*

By using the analysis method previously described for analytically solving equation (18), the theoretical tip penetration and maximum repulsive force were determined as a function of Z_{eq}, W, and S for the full range of imaging parameters. After initial observations, it became apparent that the equilibrium cantilever height had little effect on the tip penetration and maximum repulsive force values. Through further analysis, it was confirmed that the maximum attractive force and steepness of the repulsive regime were the only parameters having any significant effect on the results. In Table 4.1, the values of tip penetration and maximum repulsive force are shown for the lowest and highest equilibrium heights used in the study for various tip-sample interaction forces (while not included in the table, intermediate values of Z_{eq} were used and produced similar results).

W [nN]	S [nN/nm^2]	Tip Penetration [nm]				Force [nN]			
		Z = 15 nm	Z = 125 nm	Difference [nm]	Percent Change [%]	Z = 15 nm	Z = 125 nm	Difference [nm]	Percent Change [%]
0.5	5	0.4793	0.4814	-0.0021	0.44	0.6485	0.6589	-0.0104	1.60
0.5	750	0.0536	0.0538	-0.0002	0.37	1.6527	1.6669	-0.0142	0.86
0.5	1500	0.0402	0.0403	-0.0001	0.25	1.9198	1.9357	-0.0159	0.83
25	5	3.0802	3.1207	-0.0405	1.31	22.4391	23.6945	-1.2554	5.59
25	750	0.2906	0.2917	-0.0011	0.38	38.3209	38.8155	-0.4946	1.29
25	1500	0.2132	0.214	-0.0008	0.38	43.1926	43.6945	-0.5019	1.16
50	5	4.3127	4.3849	-0.0722	1.67	42.9968	46.137	-3.1402	7.30
50	750	0.3979	0.3996	-0.0017	0.43	68.7382	69.7453	-1.0071	1.47
50	1500	0.2906	0.2917	-0.0011	0.38	76.6418	77.631	-0.9892	1.29
		Average		-0.0133	0.62			-0.8254	2.38
		Min		-0.0722	0.25			-3.1402	0.83
		Max		-0.0001	1.67			-0.0104	7.30

Table 4.1 - Effect of Z_{eq} on theoretical tip penetration

As illustrated in Table 4.1, the absolute and relative variations in tip penetration, as the equilibrium height changes from 15 nm to 125 nm, are insignificant. This is due to the small tip-sample interaction forces that occur when the tip-sample separation is large. In Figure 4.1, a tip-sample interaction curve with a maximum attractive force of 50 nN is shown. Under this condition, the long range attractive forces between the tip and sample are experienced for the largest tip-sample separation.
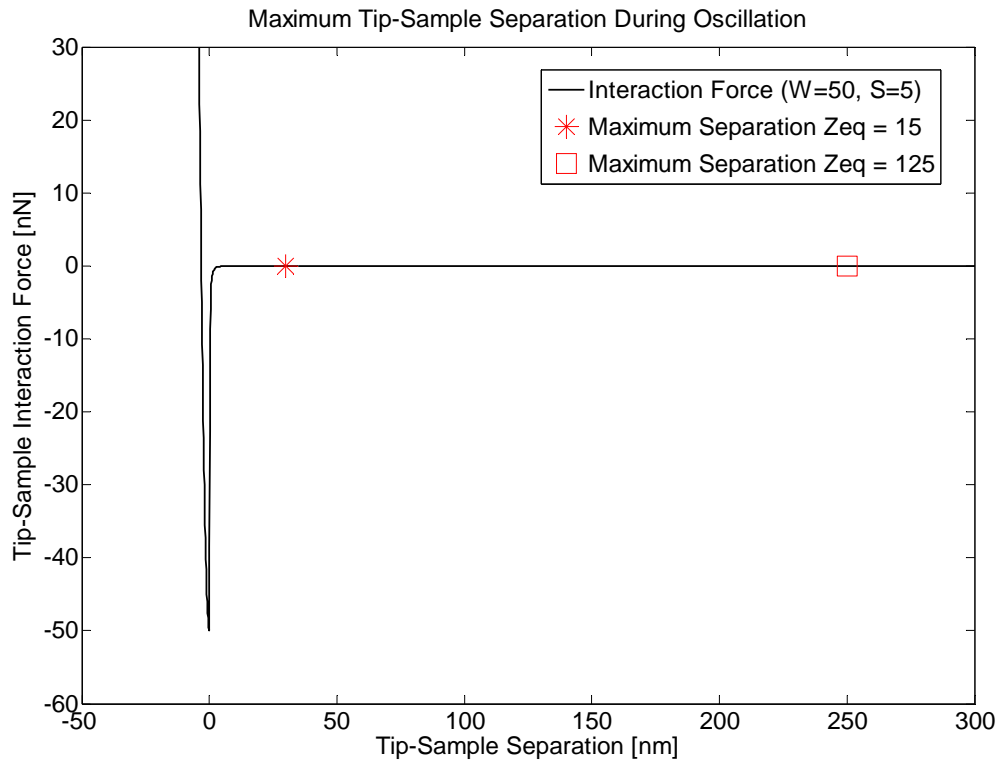
Figure 4.1 - Tip-sample interaction forces experienced during full oscillation. Where Z_{eq} is in nm, W in nN and S in nN/nm^2

The '*' marker indicates the maximum tip-sample separation during imaging if an equilibrium cantilever height of 15 nm is used. The '□' indicates the same value if the equilibrium cantilever height is 125 nm. As illustrated, the tip experiences minimal tip-

sample interaction forces in the region only traveled during large amplitudes. Since the

term inside the integral of equation (18), $F_{ts}[Z_{eq} + A_o \cos(\varphi)] * \cos(\varphi)$, is small when the

tip-sample interaction forces are negligible, the added region only has a minimal

contribution. Figure 4.2 is identical to the graph shown in Figure 4.1, except that it

contains an expanded view near the y-axis. This graph demonstrates that there are

interaction forces over the added region when Z_{eq} is 125 nm. However, these forces are

on the order of 0.001 nN compared to the maximum attractive force of 50 nN.
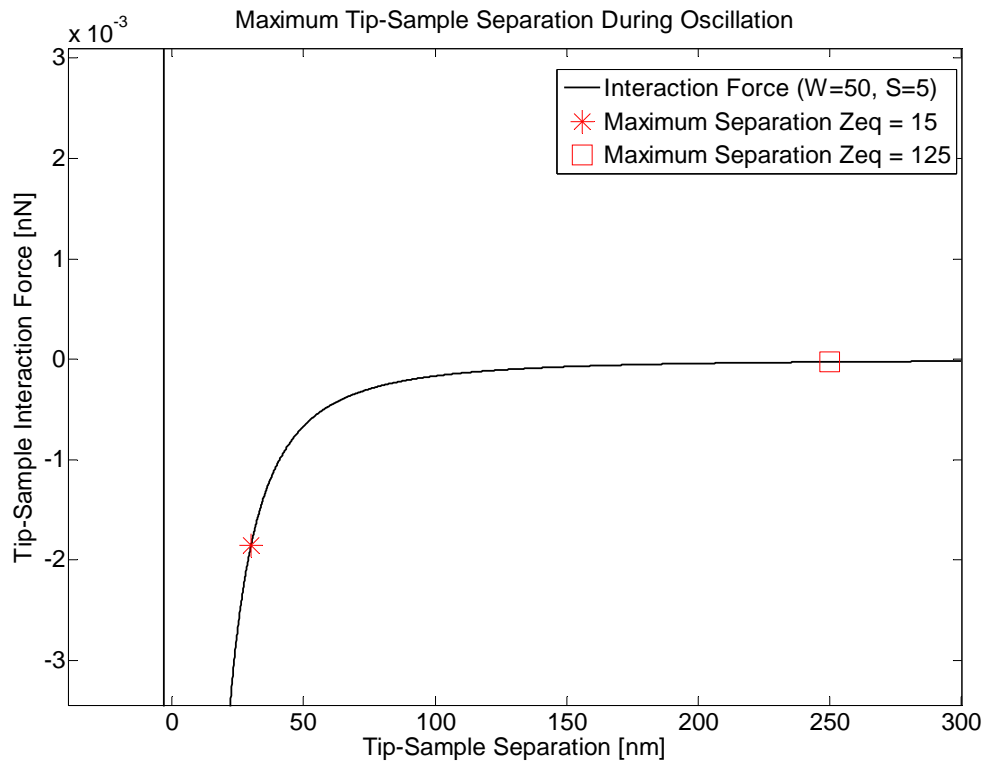
Figure 4.2 - Expanded view of tip-sample interaction forces experienced during full oscillation.
Where Z_{eq} is in nm, W is in nN and S is in nN/nm^2

After determining that the theoretical tip penetration and maximum repulsive force are only a function of the maximum attractive force and the steepness of the repulsive regime, it was important to understand what influences these parameters had on the results. In Figure 4.3, the variation of the tip penetration is illustrated as a function of both W and S over the ranges used in the study.
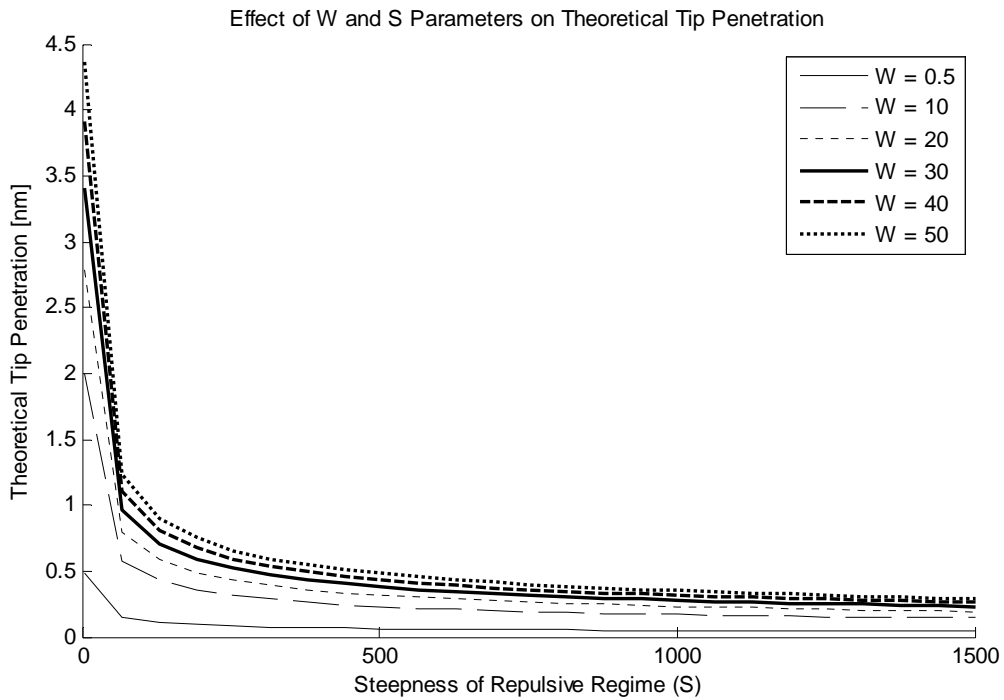
Figure 4.3 - Theoretical tip penetration values as a function of maximum attractive force (W) in nN and repulsive regime steepness (S) in nN/nm^2.

As expected, the tip penetration increases as the maximum attractive force increases and the repulsive regime steepness decreases. This is due to the fact that a resonance frequency shift of zero occurs when the tip-sample interaction force gradient is zero. Therefore, higher maximum attractive forces require higher repulsive forces to offset the attractive forces. These higher repulsive forces occur when the tip penetrates

deeper into the sample. When the repulsive regime steepness is low, the tip must penetrate deeper than is necessary with high steepness values in order to experience the necessary repulsive forces. The maximum repulsive force was determined by evaluating equation (13) at the tip penetration value. In Figure 4.4, it is shown how the maximum repulsive force varies with W and S. As previously explained, the maximum repulsive force is greater with increasing maximum attractive force and increasing repulsive regime stiffness.
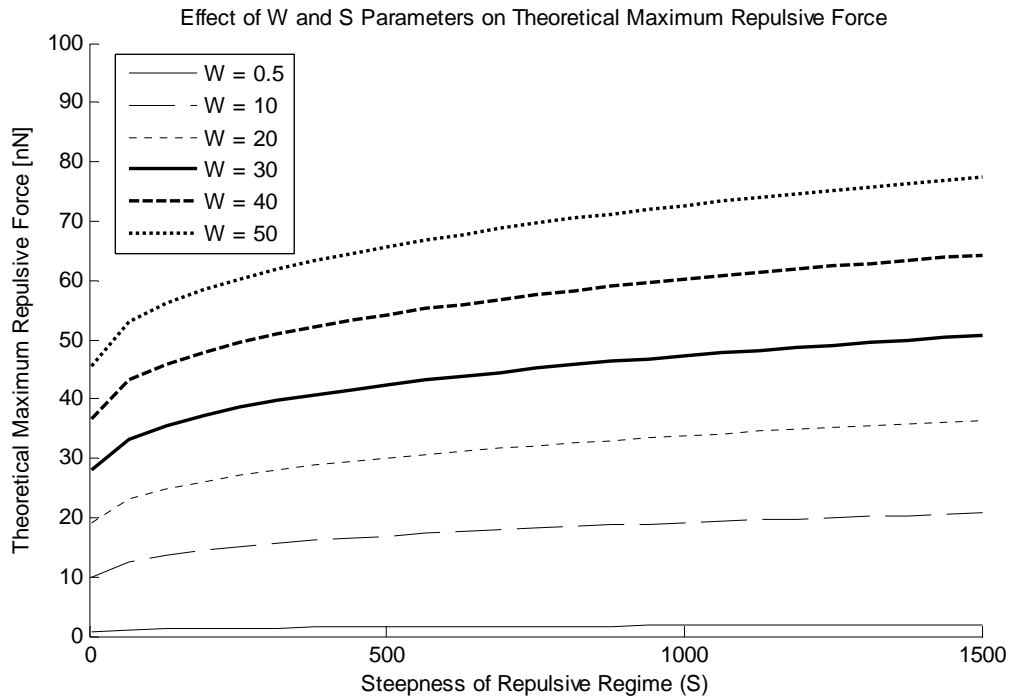
Figure 4.4 - Theoretical maximum repulsive force values as a function of maximum attractive force (W) in nN and repulsive regime steepness (S) in nN/nm^2.

4.2   *Simulation Results*

The point-mass spring model equation of motion, equation (8), was solved numerically for a range of different imaging conditions. This process verified which imaging conditions could be accurately modeled using the theoretical frequency shift equation. In addition to the initial 486 imaging combinations run, other intermediate values of the imaging parameters were examined to ensure the absence of abnormalities in these results. With over 700 separate conditions, the amount of available data could not all be presented within the context of this thesis. Various graphs showing the tip penetration values for select imaging conditions are contained in Figure 4.5. The data given in Figure 4.5 can be used to examine the effect each parameter appears to have on the maximum tip penetration. Each graph illustrates the dependence of the quality factor, force constant, and maximum attractive force on the tip penetration. By comparing the graphs, the dependence on both the equilibrium height and repulsive regime steepness can also be observed.
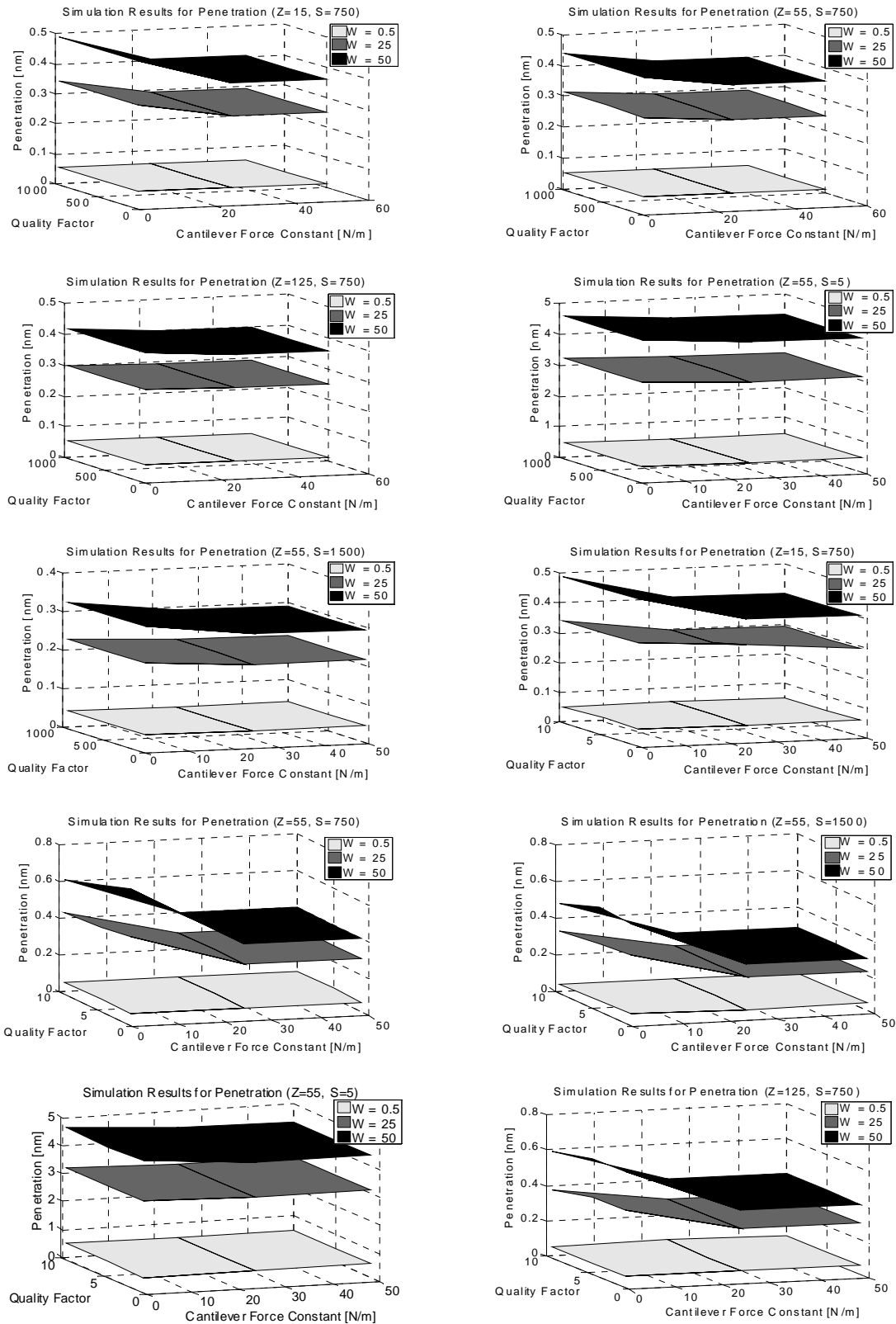
Figure 4.5 - Graphs of tip penetration values as a function of k, Q, and W for various values of Zeq and S in both air and liquid. Where Z_{eq} is in nm, W is in nN, and S is in nN/nm².

40

4.3 _Verification of Theoretical Results Through Simulation Data_

4.3.1 Initial Observations on Accuracy of Theoretical Model

The simulation results and theoretical results were in excellent agreement for all initial imaging combinations examined with force constants at 25 or 50 N/m. The maximum difference between the simulation and theoretical penetration values were 4% in air and 9% in liquid, yet a large majority of conditions resulted in variations of less than 1% in both media. Such variations led to differences in penetration values equaling only a fraction of an Angstrom. However, comparisons of the simulation and theoretical penetration values for force constants of 1 N/m produced conflicting outcomes. Observations revealed that for all low value force constant conditions in which the maximum attractive force was low, the variation between the theoretical and simulation results were less than 10%. However, for maximum attractive force values of 25 and 50 nN, the variation was as high as 40% in air and 90% in liquids. Since the maximum repulsive force is directly calculated from the tip penetration value, only the penetration will be examined for the remainder of the theoretical verification section.

4.3.2 Low Force Constant Analysis

The irregularities in sample deformation for 1 N/m force constants required a more in-depth examination into what physically occurred when using soft cantilevers. Under conditions in which the imaging medium was air ($50 \leq Q \leq 1000$), two trends were evident when determining sample deformation for force constants between 1 and 5 N/m. First, the agreement between simulation and theoretical penetration values improved as

the force constant increased. Second, increasing the cantilever equilibrium height also improved the agreement between the simulation and theoretical values. Trends for the maximum tip-sample interaction forces (W=50, S=1500) are illustrated in Figure 4.6. These tip-sample interaction parameter values were chosen because the maximum deviation in penetration results occurred with the highest interaction forces. The same trends occurred at lower steepness and maximum attractive force values of 750 nN/nm^2 and 25 nN, respectively.
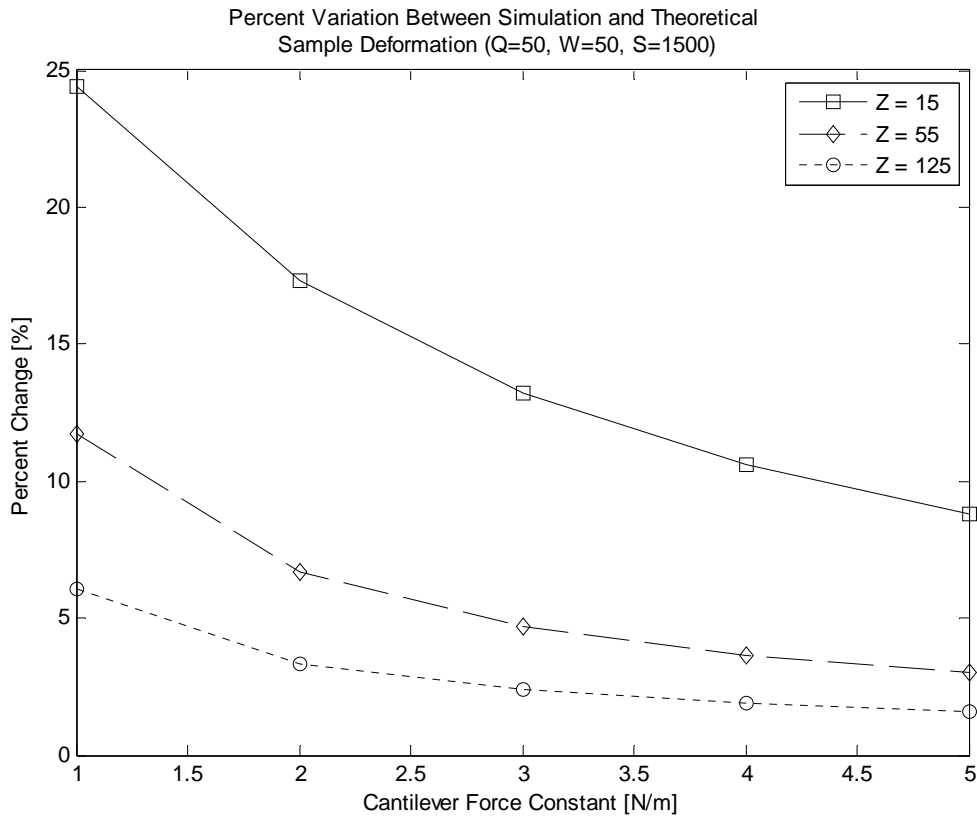
Figure 4.6 - Agreement between simulation and theoretical tip penetration values in air. Where Z_{eq} is in nm, W is in nN, and S is in nN/nm^2.

The highest deviation occurs with low amplitudes, low force constants and high attractive forces. Under these conditions, the ratio of tip-sample attractive force to cantilever restoration force is highest. The maximum restoration force occurs when the tip is furthest from the cantilever equilibrium height and is equal to

$$F_{restore, \; max} = k*(A_o - Z_{eq}) \tag{27}$$

When $F_{restore, \; max}$ is much greater than the maximum attractive force, the weakly perturbed harmonic oscillator assumption used in developing equation (12) is satisfied. Under the conditions in question, this requirement is not met since the restoration force is smaller than the maximum attractive force. In addition to producing anharmonic motion, a large ratio can cause the cantilever to "stick" to the sample. This occurs when the sum of the restoration force and the excitation force are not enough to overcome the tip-sample attractive force, causing the AFM tip to be trapped in the interaction force attractive well. However, an examination of the AFM tip trajectory showed that this phenomenon did not occur for any of the imaging parameter combinations used. Based on the worst-case-scenario findings shown in Figure 4.6, a force constant of at least 5 N/m should be used when imaging highly attractive tip-sample combinations in air. This will ensure that the sample deformation can be properly explained by the theoretical model.

When conducting the same low force constant analysis in liquid, the agreement between simulation and theoretical sample damage also improved with increasing force constants. However, an increase in cantilever equilibrium height did not necessarily guarantee better agreement. In Figure 4.7, the percent variation for the same imaging parameters as above is shown, except with a liquid imaging medium corresponding to a quality factor of 1.
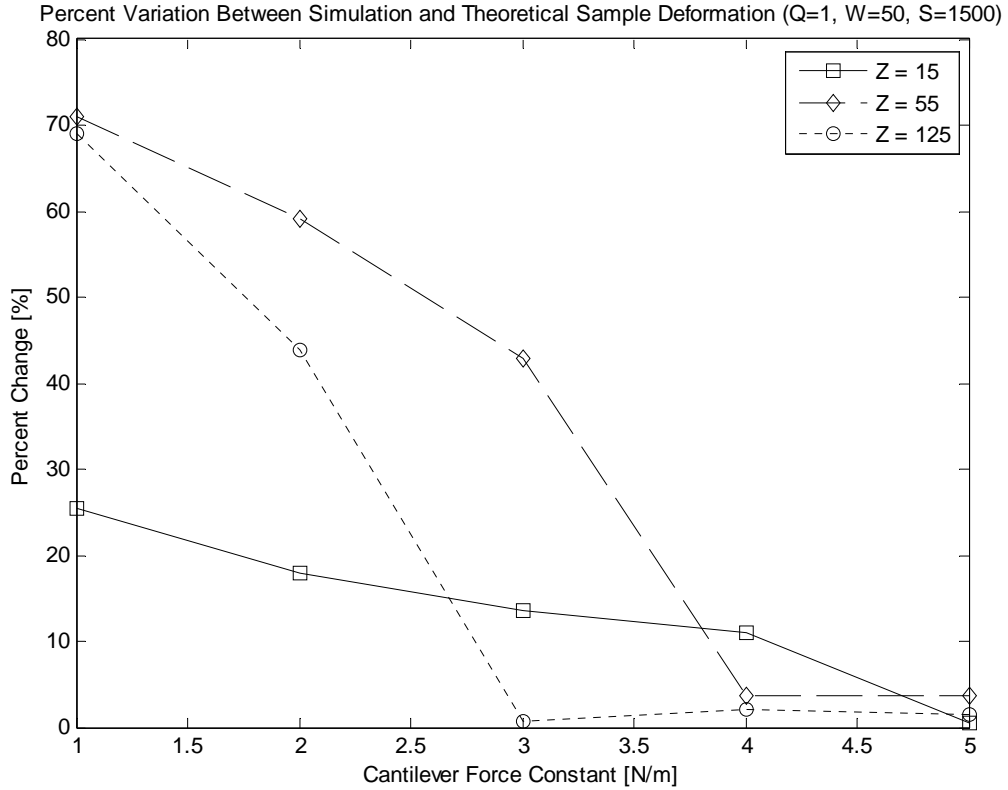
Figure 4.7 - Agreement between simulation and theoretical tip penetration values in liquid. Where Z_{eq} is in nm, W is in nN, and S is in nN/nm^2.

These findings suggest that a phenomenon occurs at low force constants and low quality factor conditions to produce results that are inconsistent with those observed for other imaging conditions. The next chapter was added to discuss preliminary findings on how discontinuities in the excitation force cause instabilities in the motion of the AFM tip. These instabilities appear to cause the inaccurate tip penetration values. A proposed solution to the instabilities is also discussed in the next chapter, which discusses future work. Despite the inconsistencies in tip penetration values, the low force constant analysis proved that a force constant of at least 5 N/m is required to ensure that the theoretical model accurately predicts the sample deformation when using highly attractive tip-sample combinations in liquid.

4.3.3 Conclusions on Accuracy of Theoretical Model

From the low force constant analysis it was determined that in order to ensure the theoretical model accurately predicts the sample deformation during steady-state oscillations within 10% accuracy, a force constant of at least 5N/m must be used. An improved level of accuracy was shown to exist when the cantilever force constant was further increased. However, the many sources of error and resolution limitations of the AFM suggest that an error of 10% is acceptable (an extended discussion on the sources of error is included in a later section). Therefore, any conclusions on the ability to quantitatively predict sample deformations and maximum tip-sample repulsive forces are only valid for imaging parameters listed in Table 3.1 and force constants of at least 5 N/m. In addition to the imaging parameter combinations discussed above, it is important to note that all intermediate imaging parameter combinations (with the exception of those having a force constant less than 5 N/m), showed the same agreement with the theoretical results.

4.4 *Correlation Between Tip Penetration/Maximum Repulsive Force and Interaction Forces*

With verification of the theoretical frequency shift equation's accuracy for the imaging parameter ranges described above, equation (12) could be used to determine tip penetration for the FFM control scheme. Given the fact that k and Q drop out of equation (12) when $\Delta f = 0$ and Table 4.1 proves Z_{eq} is not a determining factor, it became evident that the only factors affecting the sample deformation, and consequently the maximum

tip-sample repulsive force, were those parameters defining the tip-sample interaction forces. Therefore, the penetration depended only on the maximum attractive force and the steepness of the repulsive regime. In order to obtain quantitative predictions of the sample deformation in terms of these parameters, the penetration values for varying values of W and S were calculated by using equation (18) and the previously described analytical methods. By using a nonlinear multiple regression solver [44], the most accurate way to represent the theoretical results was found to be through the use of the three parameter power model of the form $y(x_1, x_2) = a * x_1^b * x_2^c$. The coefficient of multiple determination (R^2), a metric for calculating the accuracy of the regression model, was highest with this model and produced a value of 0.99985. The three parameter power model solution for the penetration as a function of the maximum attractive force and the repulsive regime steepness is

$$\rho(W, S) = 1.429 * W^{0.4802} * S^{-0.4757} \qquad (28)$$

By substituting the penetration equation into the tip-sample interaction force model, equation (13), the maximum repulsion force experienced for a given value of W and S can be expressed as

$$F_{repulsive,max}(W, S) = -W + S * (1.429 * W^{0.4802} * S^{-0.4757})^2 \qquad (29)$$

which can be simplified to

$$F_{repulsive,max}(W, S) = -W + 2.042 * W^{0.9604} * S^{0.0486} \qquad (30)$$

where $F_{repulsive,max}$ is the maximum repulsive force experienced during the operation.

4.5 *Accuracy of Regression Model*

As with any regression model, there are inherent errors between the actual penetration value and that determined by the model. There are multiple metrics which must be examined to determine how accurately the regression model can predict the maximum tip penetration during steady state oscillations. The first metric was the difference in penetration values. The graph in Figure 4.8 reflects the difference in tip penetration values for multiple values of W and S. The largest deviation between the theoretical and regression models occurs when the steepness value is low and the maximum attractive force value is high. However, this variation never exceeds 0.025 nm.
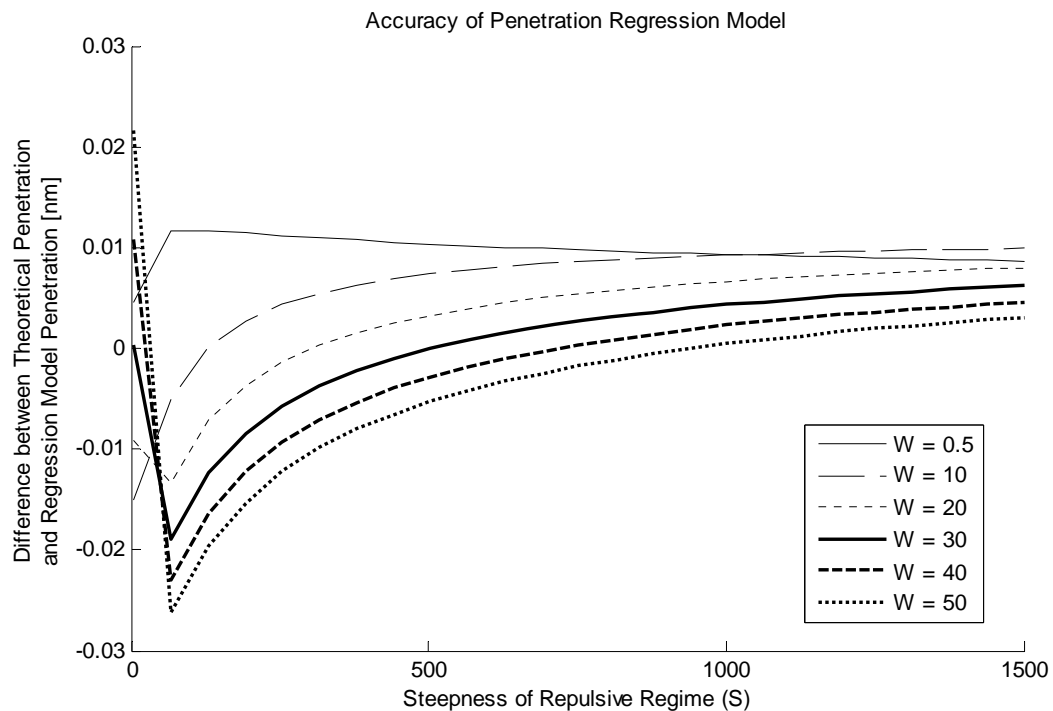
Figure 4.8 - Difference in tip penetration values between the theoretical and regression model predictions as a function of maximum attractive force and repulsive regime steepness. Where W is in nN and S is in nN/nm^2.

Considering the maximum vertical resolution and inherent sources of error in AFM, this error is believed to be more than acceptable. It has been determined that under most imaging conditions, the vertical resolution is no smaller than 0.1 nm [46-50]. Therefore, the regression models provide an accuracy at least four times greater than the vertical resolution of most AFMs. It is important to note that the vertical resolution could decrease to 0.001 nm under ideal conditions where the decay length of the frequency shift is minuscule and the signal-to-noise ratio is large [51]. Also, vertical resolutions of 0.01 nm have been experimentally achieved [10]. However, such low resolutions are only observed in non-contact mode in a vacuum, which is needed for true atomic resolution. Since FFM is not intended for use in achieving true atomic resolution and operates in a tapping mode, it is reasonable to assume a vertical resolution of no more than 0.1 nm. Various sources of error during AFM operation include, but are not limited to, signal noise, thermal drift, calibration error, small nonzero frequency shifts, laser alignment error, and tip contamination. With so many potential sources of error, it is unrealistic to assume that a more accurate regression fit would lead to experimental tip penetration values within hundredths of an Angstrom of the theoretical value.

While the absolute error in penetration values is acceptable, this cannot be the only measure of accuracy. With tip penetration values ranging from 0.0403 nm to 4.3705 nm, an error of 0.025 nm has a much greater impact if the total penetration is 0.0403 nm versus if it is 4.3705 nm. Therefore, it was also necessary to examine the percentage by which the theoretical and regression values vary. In Figure 4.9, the percent change is illustrated for the same values of W and S as above.
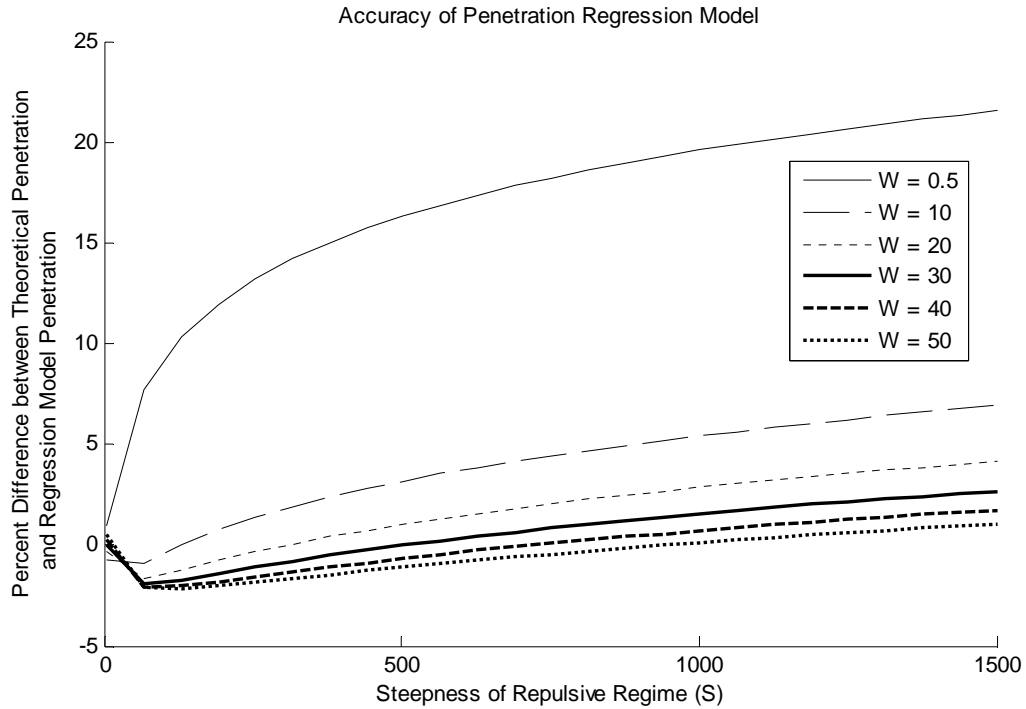
Figure 4.9 - Percent change in tip penetration values between the theoretical and regression model predictions as a function of maximum attractive force and repulsive regime steepness. Where W is in nN and S is in nN/nm^2.

In contrast to the trends observed for the absolute difference, a greater percent variation was observed for increasing repulsive regime steepness and decreasing maximum attractive force values. This is due to the fact that the total penetration was smaller under these conditions. Consequently, slight deviations in penetration result in higher relative changes. Maximum attractive forces of at least 10 nN experienced percent changes of no more than 5%, demonstrating good accuracy of the regression model. However, the percent variation jumps to over 20% for a 0.5 nN maximum attractive force value. In Figure 4.10, it is shown as to how the percent change depends on the maximum attractive force with greater resolution between 0.5 nN and 10 nN.
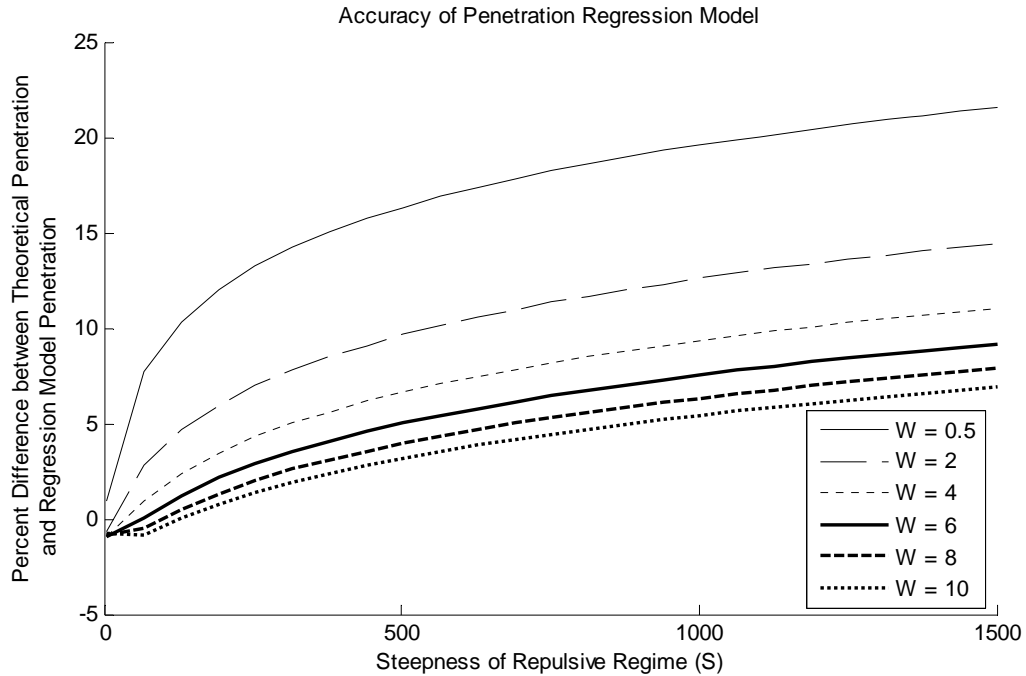
Figure 4.10 - Percent change in tip penetration values between the theoretical and regression model predictions as a function of maximum attractive force and repulsive regime steepness for smaller maximum attractive force values. Where W is in nN and S is in nN/nm².

The graph in Figure 4.10 reveals that a maximum attractive force of at least 6 nN is required to ensure a 90% accuracy. Therefore, it is important to consider the accuracy of the regression model when imaging hard samples with low attractive force. However, it is also important to remember that a 20% error in penetration when W=0.5 and S=1500 is an absolute error of only 0.008 nm, which is well below the vertical resolution of AFMs in tapping modes.

The absolute and percent variations in force between the theoretical and regression models are also important to consider in determining the accuracy of the model. Since the maximum repulsive force is determined by evaluating the tip-sample interaction force model, equation (13), at the tip penetration value, the variation in

maximum force is directly related to the variation in penetration. The difference in maximum repulsive force values ($\Delta F_{repulsive,\,max}$) is defined as

$$\Delta F_{repulsive,\,max} = (-W + S * \rho_T{}^2) - (-W * S * \rho_R{}^2) \qquad (31)$$

where ρ_T is the theoretical penetration value determined by equation (18) and ρ_R is the regression penetration value determined by equation (28). Equation (31) can be reduced to

$$\Delta F_{repulsive,\,max} = S * (\rho_T{}^2 - \rho_R{}^2) \qquad (32)$$

The variation in maximum repulsive force values increases as both the steepness of the repulsive regime and tip penetration increase. However, the total tip penetration was shown to decrease with increasing steepness values. In Figure 4.11, it is illustrated that the error in the regression model force calculation increases, then decreases, and eventually increases again as the steepness value rises.

Accuracy of Force Regression Model
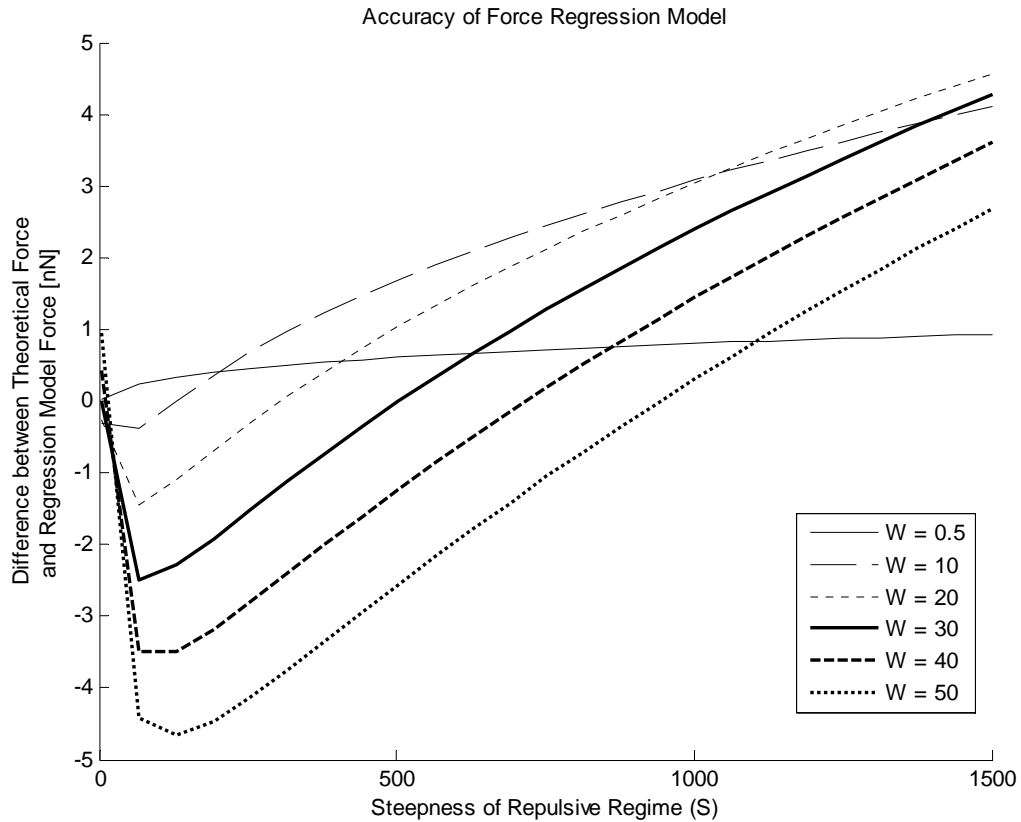
Figure 4.11 - Difference in maximum tip-sample repulsive force values between the theoretical and regression model predictions as a function of maximum attractive force and repulsive regime steepness. Where W is in nN and S is in nN/nm².

The regression model is shown to predict the maximum repulsive force with an error of less than 5 nN. With maximum repulsive force values ranging from 0.66 nN to 76.6 nN, relative variation between theoretical and regression models again became important. In Figure 4.12, the relative change in maximum repulsive force values is shown for the same values of W and S.
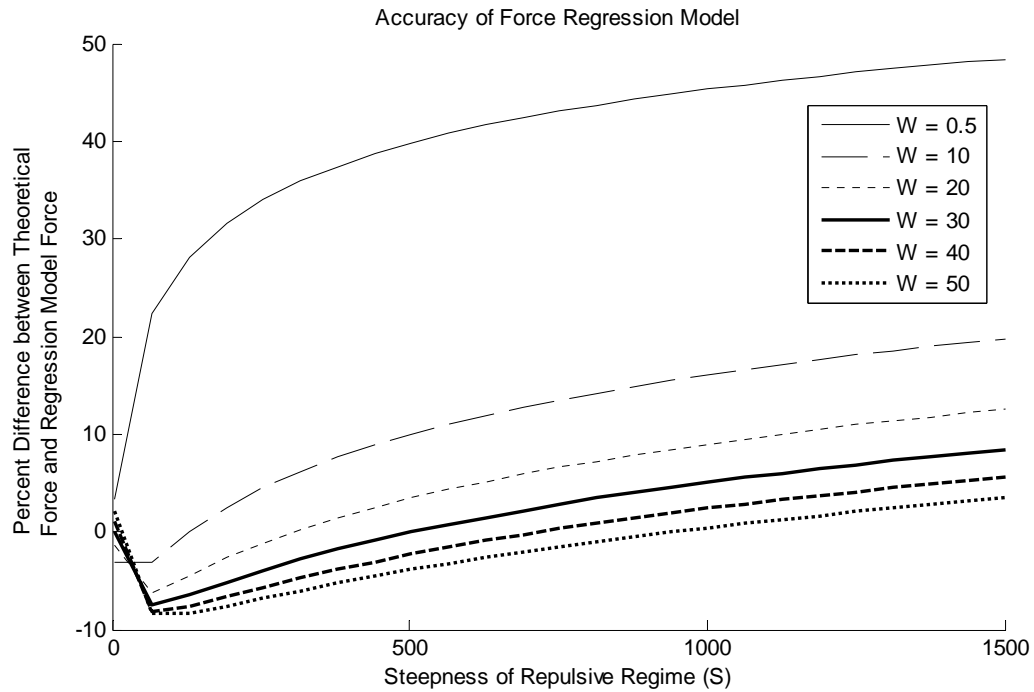
Figure 4.12 - Percent change in maximum tip-sample repulsive force values between the theoretical and regression model predictions as a function of maximum attractive force and repulsive regime steepness. Where W is in nN and S is in nN/nm^2.

In contrast to the absolute error in forces, the relative error decreases with an increasing maximum attractive force. A continuous increase in relative error is also observed as the steepness of the repulsive regime increases. As noted with the percent change in tip penetration values, a large jump occurs between maximum attractive force values of 0.5 nN and 10 nN. A graph containing maximum attractive force values within this range is shown in Figure 4.13.
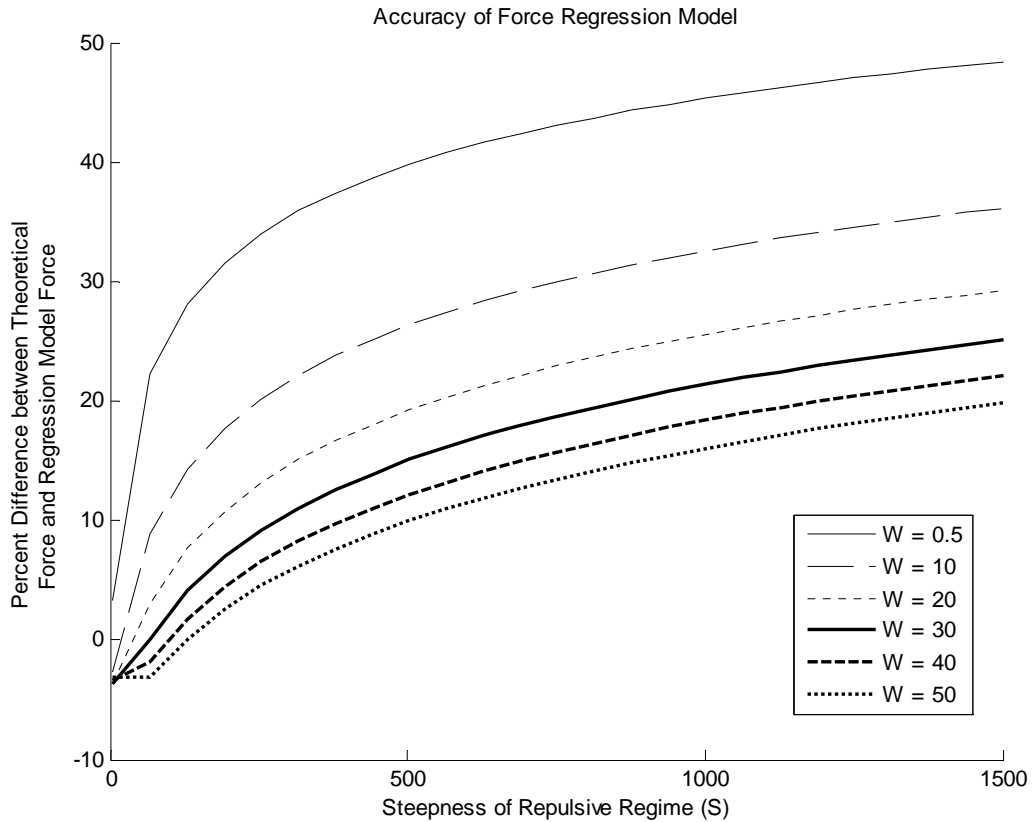
Figure 4.13 - Percent change in maximum repulsive force values between the theoretical and regression model predictions as a function of maximum attractive force and repulsive regime steepness for smaller maximum attractive force values. Where W is in nN and S is in nN/nm².

The high relative error for low maximum attractive forces suggests that the proposed regression model is inadequate for describing the maximum repulsive force experienced by the sample when the tip-sample attractive forces are low. However, the regression model can still be used to roughly estimate the repulsive forces between a tip and sample, since the absolute error in this region is as small as 0.5 nN and 3 nN for maximum attractive forces of 0.5 nN and 10 nN, respectively, as shown in Figure 4.11. Nevertheless, the user must remain aware of the potential errors in applying the regression model when low attractive forces are present.

The accuracy analysis of the regression model indicates an excellent agreement with the theoretical results for determining tip penetration values with imaging conditions between the range of acceptable imaging parameters. Therefore, equation (28) proves to be an accurate method of predicting the sample deformation during steady-state oscillation under zero frequency shift conditions. When using equation (28) to determine the maximum repulsive force by way of equation (30), the accuracy of the model decreases for low maximum attractive force values. It is also recommended that the regression model only be applied for predicting forces when the maximum attractive force is high or only approximate estimations are required.

4.6 *Piecewise Regression Model*

To increase the accuracy of quantitative predictions for the maximum tip-sample repulsive force, a piecewise function was developed. In this model, the same regression equation as proposed above, equation (30), was used for large maximum attractive forces while a new equation was determined to represent the maximum repulsive force for small maximum attractive forces. Various cutoff values of W were used in the attempt to find the value resulting in the lowest relative error for all interaction force combinations. Through trial and error, it was determined that maximum attractive forces greater than 12 nN should be modeled using equation (30). For maximum attractive forces of 12 nN and below, a new regression equation was created using a multiple correlation regression solver [44]. The piecewise regression force model became

$$
\begin{aligned}
F_{repulsive,\max}(W,S) &= 0.9903 * W^{0.8282} * S^{0.1526} & W \leq 12 \\
F_{repulsive,\max}(W,S) &= -W + 2.042 * W^{0.9604} * S^{0.0486} & W > 12
\end{aligned}
\tag{33}
$$

4.7   *Accuracy of Piecewise Model*

The same metrics as those used to determine the accuracy of the first force regression model are applied to the piecewise regression model. First, the absolute error between the piecewise regression and theoretical values is shown in Figure 4.14. The maximum attractive force values have been changed in order to show more values less than 12 nN to demonstrate the increased accuracy of the piecewise model. The absolute errors for W = 30 and 50 nN remain unchanged since equation (30) is still used in calculating the maximum repulsive force under those tip-sample interaction forces. However, the error associated with the other values of W has decreased.
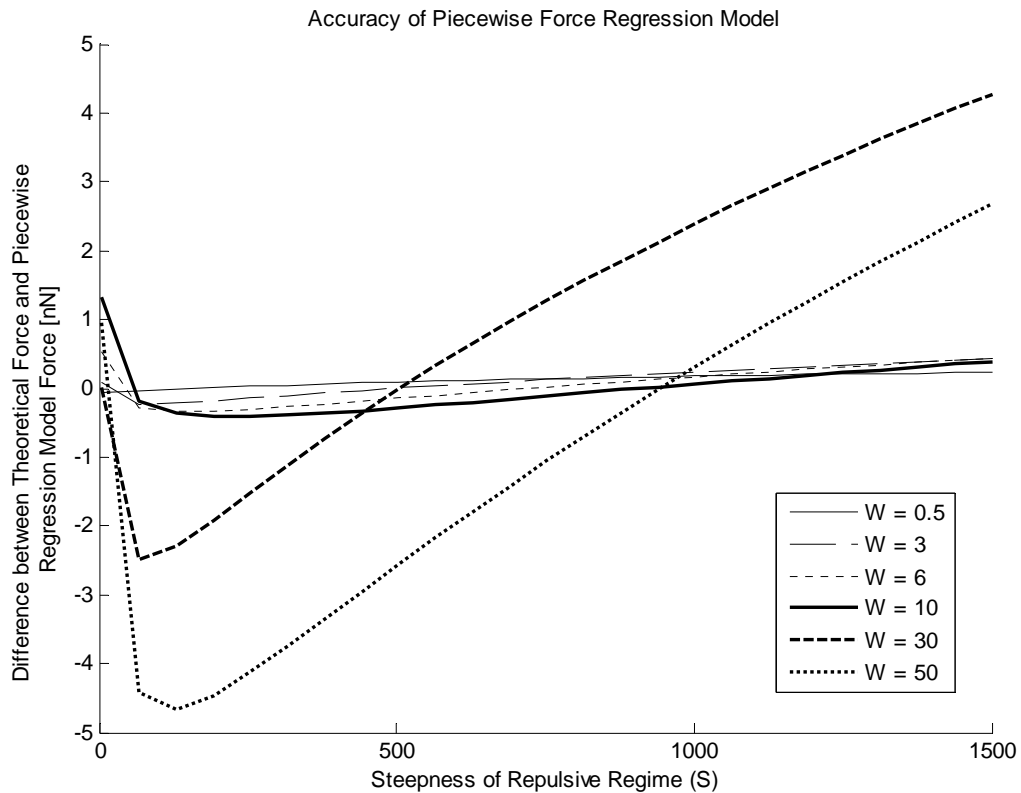
Figure 4.14 - Difference in maximum tip-sample repulsive force values between the theoretical and piecewise regression model predictions as a function of maximum attractive force and repulsive regime steepness. Where W is in nN and S is in nN/nm².

The relative error reveals the most significant improvement in accuracy over the unified model. The percent variation between the theoretical and piecewise models remains below 15% for all tip-sample interaction forces and below 10% for most cases. Given the intrinsic errors previously mentioned and the errors in determining the tip-sample interaction force parameters, equation (33) provides a prediction of the maximum repulsive force with as high of an accuracy as can be expected.
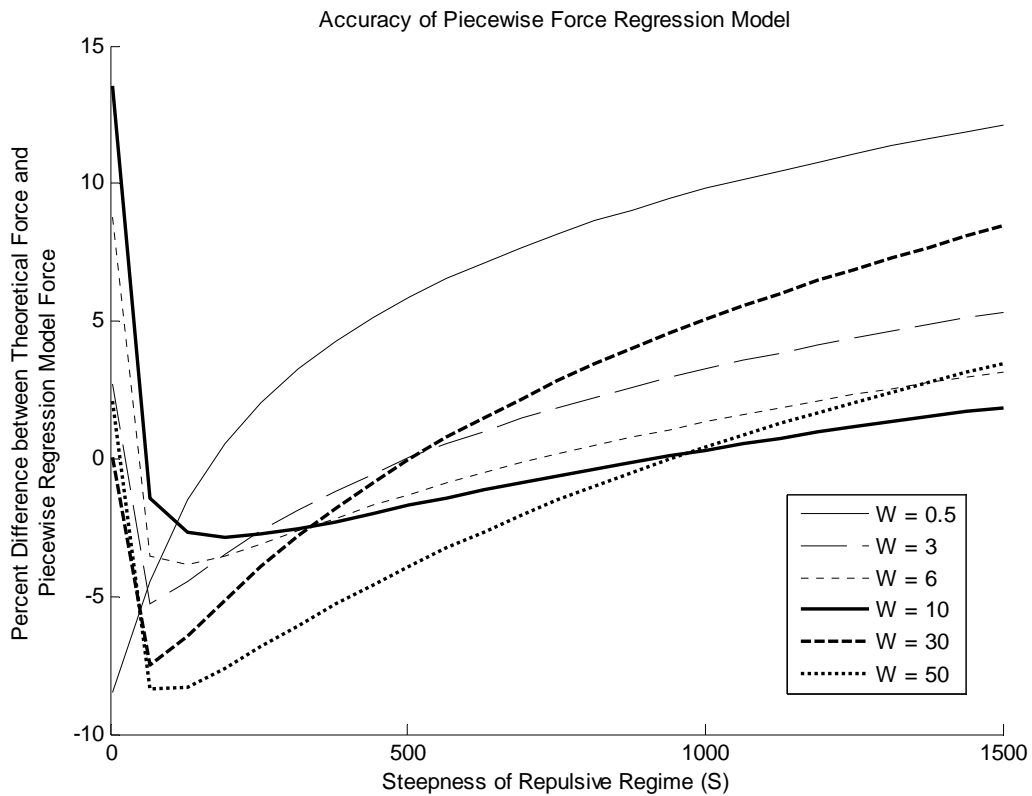
Figure 4.15 - Percent change in maximum tip-sample repulsive force values between the theoretical and piecewise regression model predictions as a function of maximum attractive force and repulsive regime steepness. Where W is in nN and S is in nN/nm^2.

4.8 *Applications*

The primary goal of this study was to examine what factors determined the maximum tip-sample repulsive force and sample deformation experienced when imaging in FFM-AFM mode with a zero resonance frequency shift. Coupling this information with a knowledge of the sample's tolerance to penetration and repulsive forces, a user could determine the likelihood of sample damage prior to imaging. Extracting the maximum attractive force and repulsive regime stiffness for a specific tip-sample interaction could be achieved in a number of ways. In many cases, the tip-sample interaction forces between the sample and the tip in use may be well known. This information may be gathered from previous experiments with the tip and sample in use or through molecular dynamic simulations. Experimental force curves of the sample can also be used to determine the necessary maximum attractive force by observing the required pull-off force when retracting the tip from the sample. The repulsive regime steepness can also be determined through experimental force curves; although, sample damage may occur if the tip penetrates too far into the sample. Having either a small area of the sample that is expendable or a separate expendable sample of the same material, the steepness could be determined for all subsequent samples of that material. Approximate steepness values can also be determined by only allowing the tip to penetrate slightly into the sample. Methods have also been developed to determine tip-sample interaction force curves over the entire sample, which could then be used to determine the repulsive forces that occur during the scan [13, 24, 57]. With a knowledge of the maximum attractive force and repulsive regime stiffness the user could either: refer to the graphs in Figure 4.3 and Figure 4.4; use the regression models provided; or

perform numeric integration of equation (18) using a similar method to the one described in this thesis.

Another potential application of this work would be in determining the location of the true skin of a sample. In the context of this thesis, the true sample skin is the topography of the sample without any sample deformation. If the interaction force parameters were known for all parts of a sample, the height trace returned by the AFM could be modified using the corresponding tip penetration values to determine the true height of the sample. In Figure 4.16, a qualitative demonstration of how varying interaction forces and tip penetration values can affect the accuracy of a height trace is provided.
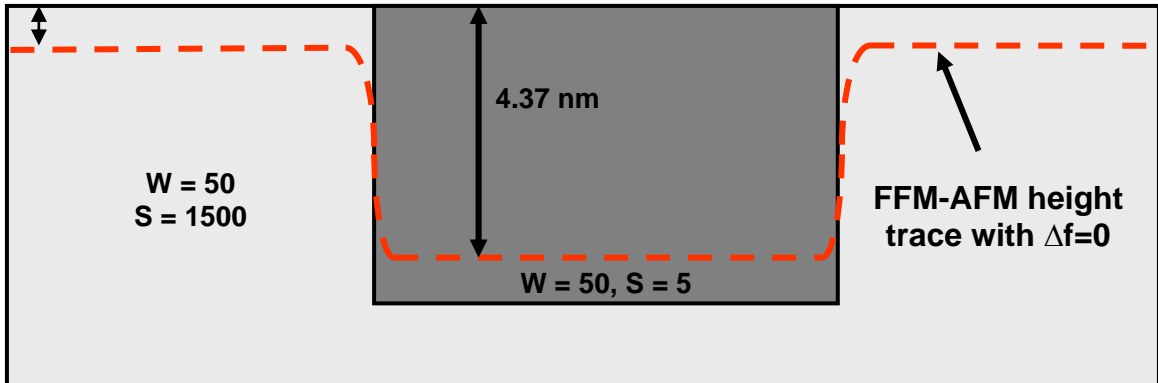
Figure 4.16 - Inaccurate height trace due to tip penetration. Where W is in nN and S is in nN/nm^2.

The example above represents extremely soft material inserted into an extremely hard material with the top surfaces of the two materials in alignment. The same concept can be applied if the top surfaces were not aligned; however, other factors of imaging over steps and trenches would also influence the penetration [58]. Nevertheless, these factors can be ignored in the current example. While this example serves as a worst-case-

scenario due to the extreme variation in repulsive regime steepness values, a similar effect would be observed, but to a smaller degree, if the materials where more akin in repulsive regime steepness.

As seen in Figure 4.16, the penetration into the soft sample is over 4 nm greater than the penetration into the hard sample. This gives the impression that a 4.08 nm trench exists where the softer material was inserted. If the maximum attractive force and repulsive regime steepness of both materials are known, the corresponding tip penetration values could be added to the height trace of the sample which would show that the surface is flat. While the variation in penetration heights may not be an area of concern when the materials are similar and the size of the samples are on the order of tens to hundreds of nanometers, it can be a critical factor on small scales and when vastly different materials are used, such as a soft sample on a hard substrate.

5 Future Work

5.1 *Instabilities When Using Low Force Constants in Liquid*

The inconsistent tip penetration results for low force constants and low quality factors led to a more thorough investigation into what phenomenon was causing the inaccurate results. While there is still a need for further study before the dynamics of AFM use in liquid with soft cantilevers is fully understood, the suspected cause of error is described in this section. The parameters included in Table 5.1 describe the imaging conditions of the example case used to explain the results from the preliminary study.

Imaging Parameter	Value	Unit
Equilibrium Height	55	nm
Quality Factor	1	-
Force Constant	3	N/m
Max Attractive Force	50	nN
Repulsive Regime Steepness	1500	nN/nm^2

Table 5.1 - Imaging conditions of example case for soft cantilever in liquid

For the imaging conditions described above, an adequate timestep would have been approximately 3.5 ns. However, a timestep of 0.1 ns was used to integrate equation (8) for the work below. As a result, errors in the tip penetration values were not attributed to inadequate timesteps. In addition, the PID gains were lowered significantly, to ensure that overly aggressive gains were not another cause of error. Finally, the simulation length was set to 0.5 seconds providing plenty of time for the initial equilibration time and for the excitation force to find a steady state value.

In Figure 5.1, both the response frequency and the excitation force amplitude after each oscillation are shown. These graphs show that a period of 0.1 seconds was given

without any feedback loops activated. This period of constant excitation amplitude and frequency ensured that the tip made contact with the sample. When the FFM controls were activated at 0.1 seconds, the excitation amplitude began to change so that an amplitude of oscillation could be achieved that would result in a zero frequency shift. In Figure 5.1 (a), it is shown that the free resonance frequency of 10 kHz is never reached. The frequency fluctuates between a low frequency and a high frequency oscillation, while the excitation force amplitude changes back and forth accordingly. Similar results were previously observed when the PID gains were too high. However, lowering the gains by a factor of 100 failed to produce improved results.
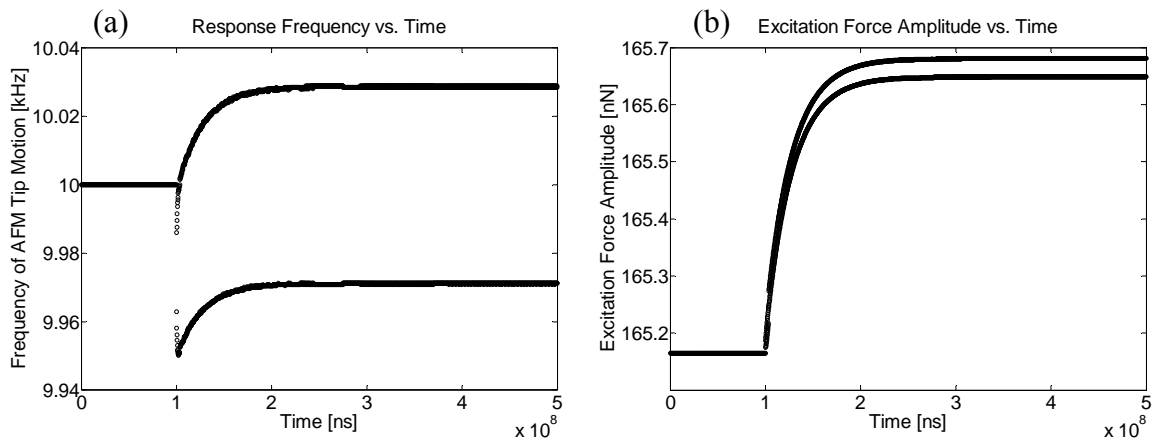
Figure 5.1 - (a) Response frequency of AFM tip after each oscillation for entire duration of 0.5 second simulation. (b) Amplitude of excitation force after each oscillation

From the trajectory plot of Figure 5.2, it is seen that the amplitude of oscillation also jumps between a high amplitude branch and a low amplitude branch. This result is qualitatively similar to the bistability effect in AM-AFM, except that both amplitudes are in the repulsive regime in this case. Some amplitude change is expected due to the changes in excitation force shown in Figure 5.1 (b). However, the linear relationship

between excitation force and amplitude should cause the change in amplitude to be approximately 0.03 nm. The observed amplitude fluctuation is approximately 10 times greater, which suggests that the change in excitation force was not the cause.
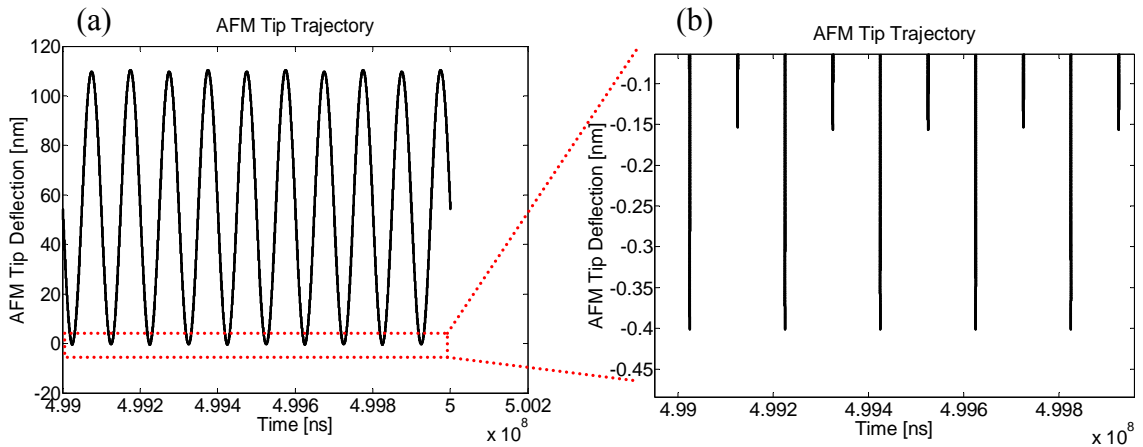
Figure 5.2 - (a) AFM tip trajectory during final 10 oscillations. (b) Expanded view of trajectory to show lowest point reached in each oscillation

Since all previous observations in this thesis related to AFM dynamics assume harmonic motion, it is vital that the external excitation remains nearly harmonic. However, it was observed that by resetting the excitation force to the maximum value after each oscillation, a harmonic excitation did not exist. In Figure 5.3, the external excitation is shown for the last 10 oscillations. By closely examining the force values near the peaks, it became evident that discontinuities existed. These discontinuities resulted in anharmonic tip motion causing large changes in amplitude despite relatively small changes in the amplitude of the excitation force.
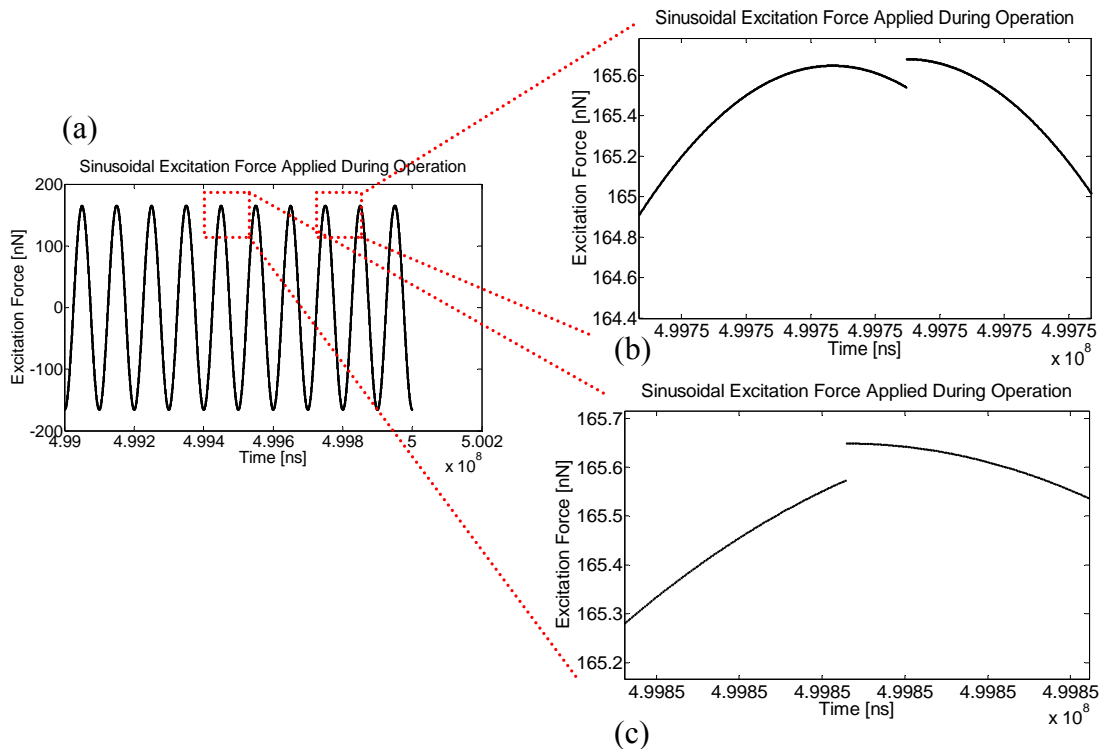
Figure 5.3 - (a) External excitation force applied during final 10 oscillations. (b & c) External excitation at peaks to show discontinuities

The imaging conditions outlined above are just one set of imaging combinations that produced results similar to those shown above. However, further research is required to fully understand when such discontinuities in excitation force cause instability in the tip motion. Work up to this point suggests that this phenomenon only occurs for low quality factors, low force constants and large tip-sample interaction forces, which is equivalent to imaging with soft cantilevers in a liquid medium using tip-sample combinations that are both highly attractive and hard. Under such conditions, the high interaction force gradient causes significant changes to the effective resonance frequencies of the soft cantilevers. Also, the low quality factor causes a quick response time that adjusts to the changes in excitation amplitude and frequency in less time than the period of oscillation. The combination of large shifts in effective resonance

frequency and fast response times appears to be the driving factor for the unstable oscillations. The range of parameters for which this occurs also appears to be dependent on the other imaging parameters. For example, when the quality factor is 7 or above, and all other imaging conditions in Table 5.1 remain constant, there are no signs of instability. However, if the force constant is lowered to 1 N/m, the lowest quality factor for which stable oscillations occur is 12. The other imaging parameters also determine if stability is achieved, as instabilities were only seen for cantilever equilibrium heights between 35 and 100 nm when using the other imaging parameters from Table 5.1. Due to the variation in conditions in which an instability occurs, an in-depth study would be required to determine exactly when and how the instabilities occur.

5.2 *Implementation of Self-Excitation*

The instabilities observed at low force constants and low quality factors is a consequence of the method used during the simulations for frequency modulation. To maintain the excitation force at the effective resonance frequency and 90 degrees ahead of the response motion, for maximum positive feedback, the excitation force is set to the maximum value when the AFM tip is at the equilibrium position. Besides producing the instabilities described in the previous section, this method also introduces problems when attempting to experimentally implement FFM-AFM. One way to eliminate the limitations associated with the current frequency modulation technique is to implement the self-driven oscillator method of frequency modulation. The self-driven oscillator is the primary method of frequency modulation in traditional FM-AFM operation [19, 26,

27, 34, 40, 59-62]. In self-driven AFM, the cantilever excitation force is directly determined by the response of the cantilever. This is in contrast to having an external excitation force sine wave consisting of a predefined amplitude, frequency, and phase. The difference in schemes is illustrated by comparing the excitation force term in the equation of motion. As shown in equation (8), the traditional method of excitation is a function of F_o and ω. However, the equation of motion with self-driven excitation is

$$m\frac{\partial^2 Z(t)}{\partial t^2} + \frac{m\omega_o}{Q}\frac{\partial Z(t)}{\partial t} + K*[Z_{eq} - Z(t)] = F_{ts} + g*K*Z(t - t_o) \tag{34}$$

where g is the gain factor and t_o is the time delay. Rather than F_o and ω, the excitation force is a function of a gain factor and the deflection of the cantilever. In FFM-AFM, the desired phase shift is 90 degrees to ensure maximum positive feedback. By setting t_o to $^1/_4$ the period of oscillation, the excitation force will lead the response by 90 degrees. The gain factor can also be determined analytically [40] by

$$|g| = \frac{1}{Q} + \frac{2*f_o}{A*K}\int_0^{1/f_o} F_{ts}[Z(t)]*\sin(2*\pi*f_o*t)dt \tag{35}$$

The implementation of this method into FM-AFM can be found in many references including [26, 27, 34, 40]. The basic operation begins by sending the cantilever deflection signal through a bandpass filter to eliminate unwanted noise. The signal is then split three ways, with one branch entering a frequency detector to determine the current frequency. This calculated frequency shift determines the height signal during imaging. The second branch of the filtered deflection signal is sent to a phase shifter which shifts the phase 90 degrees to ensure maximum positive feedback. This signal is then multiplied by the gain factor and sent to the actuator to drive the oscillation. The final filtered deflection signal is used to calculate the amplitude of the oscillation.

This information is compared to the present amplitude and the gain is then adjusted accordingly to ensure the amplitude of oscillation is constant. This process is most often completed through the use of a PI controller. In Figure 5.4, a diagram illustrating the basic components of the system for FM operation is provided.
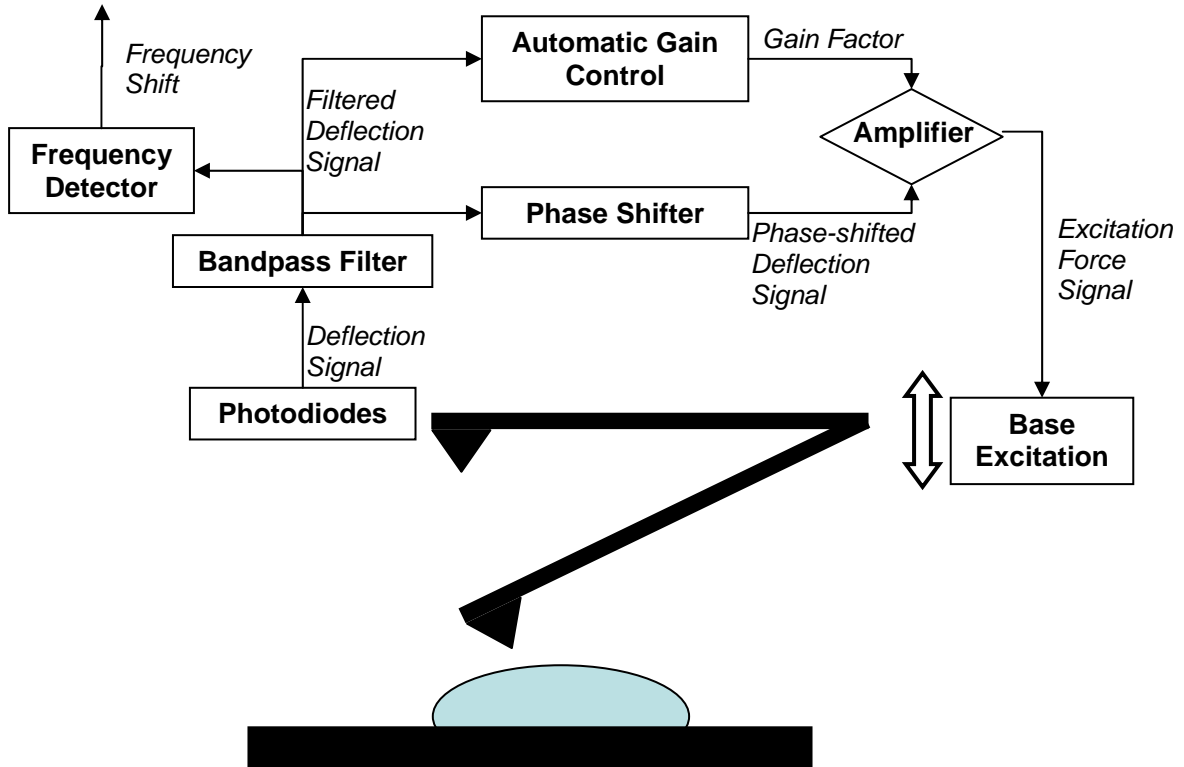
Figure 5.4 - Diagram of basic components in self-excitation FM operation

While this method works well for FM-AFM, the system will have to be adapted to implement FFM-AFM. The most significant modification will be that the Automatic Gain Control (AGC) requires both the frequency shift and amplitude as inputs to determine the appropriate gain factor. This is due to the fact that FM-AFM requires constant amplitude while FFM-AFM adjusts the amplitude throughout the scan. Consequently, the amplitude signal could be used for the height trace rather than the

signal coming from the frequency detector. The specifics of implementing FFM-AFM experimentally and specifically the self-excitation component are still in the beginning stages and more work must be done to determine all that is involved in this process. Through the implementation of self-excitation, the adjustments to changes in effective frequency should be detected and accounted for in less time than required for the current method of external excitation. In addition, the discontinuities observed in the excitation force for externally driven oscillators can be eliminated, which should improve the stability at low force constant and low quality factor conditions.

6 Discussion and Conclusions

Despite the extensive research on the relationship between the shift in resonance frequency and the tip-sample interaction forces, the resultant sample deformation and maximum repulsive force has remained largely unexplored. The purpose of this thesis was to provide a means to accurately and easily predict these values for a wide range of imaging conditions. The equation of motion for the point-mass spring system was solved numerically to determine which imaging conditions satisfied the assumptions made in developing the theoretical frequency shift relationship. After determining the appropriate range of imaging conditions, it was discovered that only the parameters defining the tip-sample interaction forces affected the tip penetration and maximum repulsive forces. For the interaction force model used in this study, the determining parameters were maximum attractive force and repulsive regime stiffness. Results showed that a simple three parameter power series regression model was adequate for representing the tip penetration as a function of the two interaction force parameters. However, to attain the desired accuracy for the maximum repulsive force model, a piecewise function was used.

There are multiple limitations and sources of error associated with the findings in this thesis, which should be taken into account when applying the findings. As previously mentioned, experimental AFM operation has many inherent sources of error including the following: tip and laser alignment errors; low signal to noise ratios; tip deformation and contamination; thermal drift; sample contamination; external forces and vibration; and many others. Since the tip-sample interaction force parameters will often be extracted from experimental force curves, the determination of these parameters can also introduce sources of error. These errors can occur in obtaining experimental data, as

well as fitting the experimental data to the interaction force model. Multiple force curves may need to be averaged in order to improve the accuracy of the interaction force parameters. Finally, it has been emphasized earlier that the tip penetration and maximum repulsive force predictions are for oscillations in which the resonance frequency shift is zero, meaning the interaction force gradient is zero. This is only the case when adequate time is provided for the feedback loops to adjust the excitation force amplitude until a steady-state oscillation with a zero frequency shift is achieved. If the scan speed is too high and the feedback gains are not at proper values this state may not be achieved. The tip penetration may be greater if there are drastic changes in topography [57] or if the gains are not near optimum values. Despite these shortcomings, the agreement between the well established frequency shift model, equation (12), and the numerical solution to the equation of motion suggests that the findings of this thesis provide an accurate method of quantitatively predicting sample deformation and tip-sample repulsive forces. These predicted values can be utilized in determining the probability of sample damage, which is especially important when imaging soft samples. Additionally, with a knowledge of the sample deformation, the true sample skin could be determined by adding the penetration value to the height trace throughout the scan. Accounting for the sample deformation as a component of post-processing can lead to more accurate images.

Appendix A – Experimental Work

While the focus of this thesis project was to develop a quantitative prediction method in order to gain insight into the newly developed FFM mode through simulations, some exploratory experimental work was also conducted. The main goals of the experimental activities were to gain a better understanding of experimental AFM operation in order to advance the simulation methods, and to perform an initial assessment of the obstacles that will be faced during the eventual experimental implementation of FFM. The experimental work also sought to verify some components of the work presented in this thesis, such as the validity of the tip-sample interaction potential functions used.

The process of transitioning from purely simulation-based AFM work to experimentation was done by trial and error. Having the Asylum Research MFP-3D atomic force microscope at the disposal of the research group, experiments were performed for different tip-sample combinations, and under different operating parameters. The first step was to become skilled at acquiring accurate images for standard samples. The commercial version of the MFP-3D AFM is limited in that the only available operating modes are contact and amplitude modulation, referred to as AC (amplitude control) mode on this instrument. Other operational modes are being developed by Asylum Research such as piezoforce mode, dual AC mode, and a frequency modulation mode; however, these modes are only available in pre-release versions of the operating system and are not yet commercially available. Therefore all exploratory work was performed only in contact and AC mode. Part of the learning process was to study the effect of the various parameters on image quality. This also

helped gain a better understanding of how the controls system operates in terms of feedback loops structure and speed, of the roles of the various electronic instruments within the controller, of the speed of response of the instrument, and of the influence of all of the above on overall characterization performance.

While various tip and samples were used, most of the imaging was performed on the calibration grating sample provided with the AFM. This sample contains square trenches which were 200 nm deep and 5 μm wide. Since the features of this sample were well known, the acquired images could be compared to the expected images to determine their accuracy. In Figure A. 1, a side view of a height trace of the calibration grating acquired in AC mode is shown. A top down view from the same height trace is also shown in Figure A. 2. AC mode was used for the acquisition of this height trace and the cantilever used was the Olympus AC160TS which has a silicon tip with a radius of 10 nm, a force constant of 42 N/m and a free resonance frequency of 300 kHz.
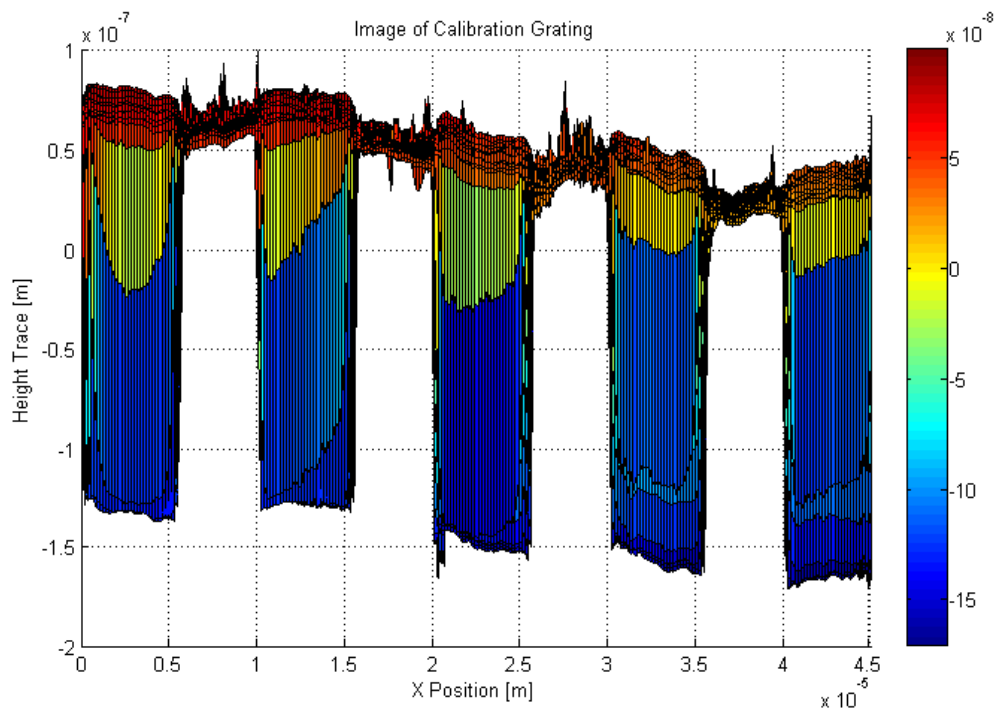
Figure A. 1 - Side view of calibration grating height trace.
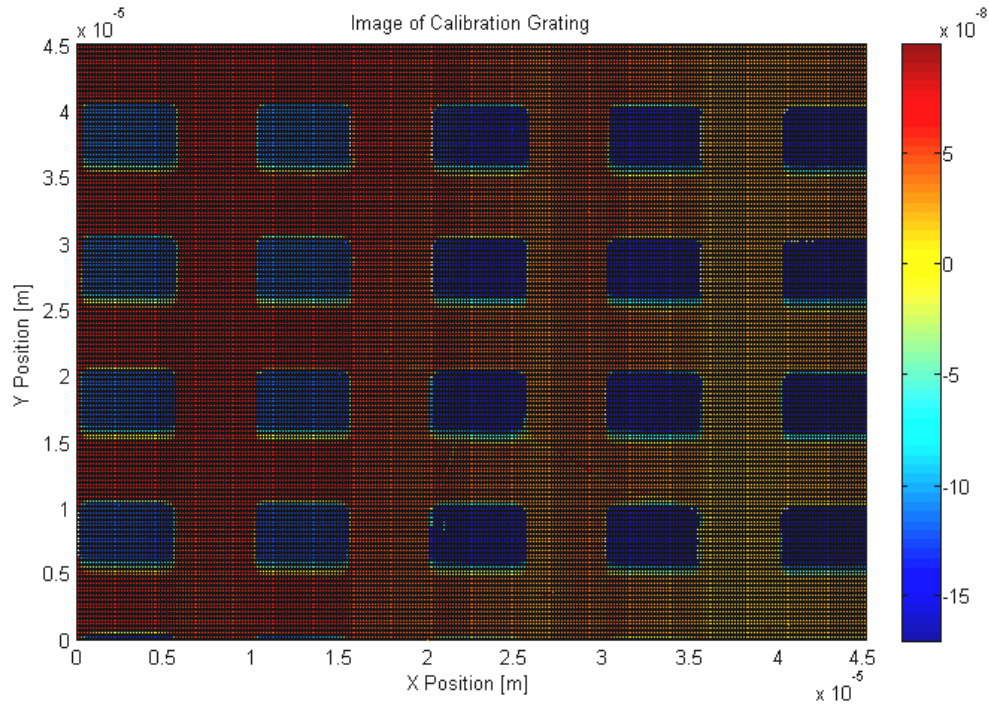
Figure A. 2 - Top view of calibration grating height trace.

As shown in Figure A. 1 and Figure A. 2 the dimensions of the trenches are in good agreement with the expected values. The AC height trace shown above is just one example of the images collected. Other cantilevers and probes were also used with lower force constants and resonance frequencies, which provided information on the effect of these parameters on the image quality.

Besides AFM imaging, force curve acquisition was another important component of the experimental AFM work. There were multiple benefits to learning how force curves are obtained in AFM. One such benefit was learning how a user would go about determining the tip-sample interaction force parameters required to predict sample deformation and the resultant repulsive forces from the quantitative prediction method developed in this thesis. Another benefit was that the tip-sample interaction force model could be compared to the experimental force curves. If the force constant of the

cantilever is known, the process for force curve acquisition on the MFP-3D is a relatively automated process with the only necessary user inputs being the maximum force reached, or "trigger point," and the speed of the tip as it approaches and retracts from the sample. An example of the instrument output is shown in Figure A. 3 for a silicon tip on a glass slide.
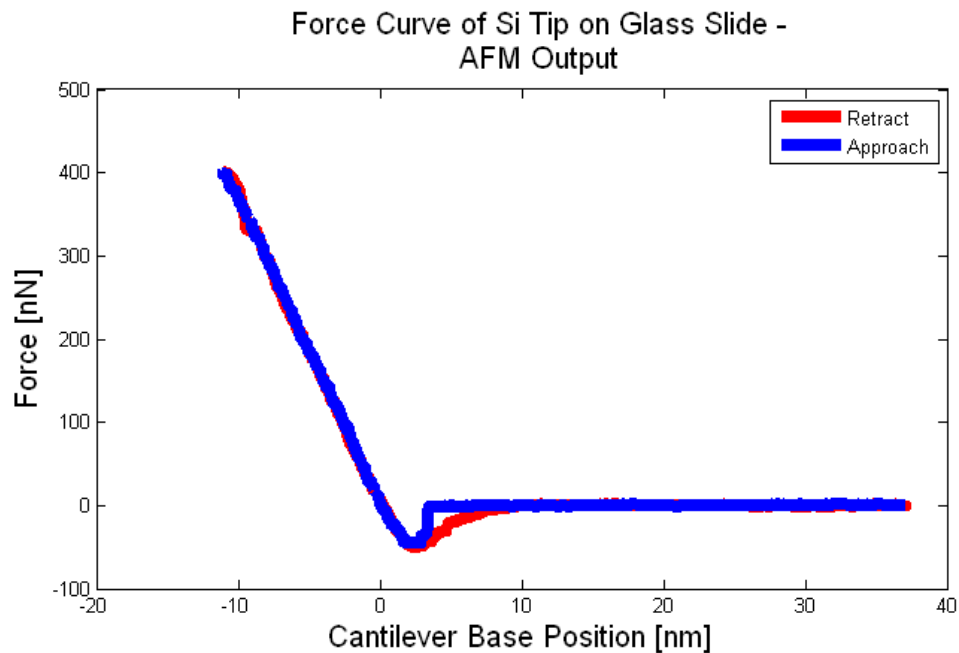
Figure A. 3 - Force curve output from AFM instrument

The graph shows the force, measured through the deflection of the cantilever, versus the cantilever base position. However, true force curves show the force versus the tip-sample separation. Therefore, it was necessary to account for the deflection of the cantilever and remove its effect from the force curve. After this process, the repulsive regime of the experimental force curve became steeper and is indicated by the red line in Figure A. 4. Only the repulsive regime of the experimental force curve is accurate due to the "jump to contact" phenomenon which occurs in the attractive regime. In Figure A. 4**,** the

74

corresponding tip-sample interaction force curve from equation (13) is also shown. The

maximum attractive force was simply determined by the minimum (i.e., most negative)

force experienced during the force curve acquisition. The steepness of the repulsive

regime value was calculated by performing a least squares regression fit of the

experimental data.
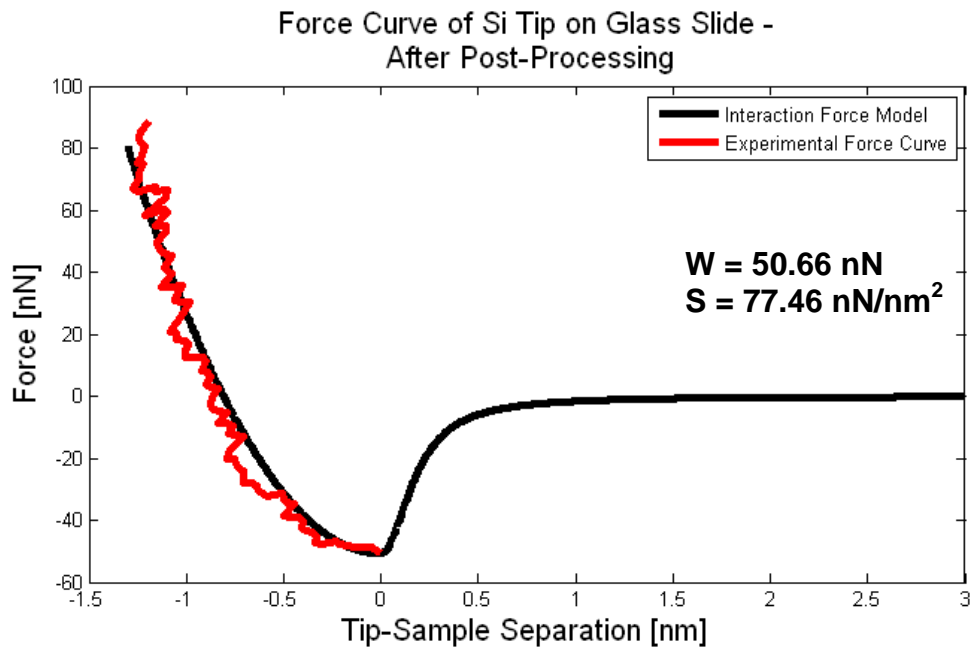
Figure A. 4 - Modified force curve to reflect tip-sample separation. The values of the maximum attractive force (W) and steepness of the repulsive regime (S) correspond to equation (13).

Since equation (13), which models the tip-sample interaction forces, was derived

by fitting the results to various molecular dynamics data, it was important to verify the

accuracy of the model experimentally. In Figure A. 5, the same experimental force curve

as above is compared to the interaction force model from equation (13) as well as the

established DMT model from equation (5). The coefficients for the DMT model were

also found by performing a least squares regression fit.
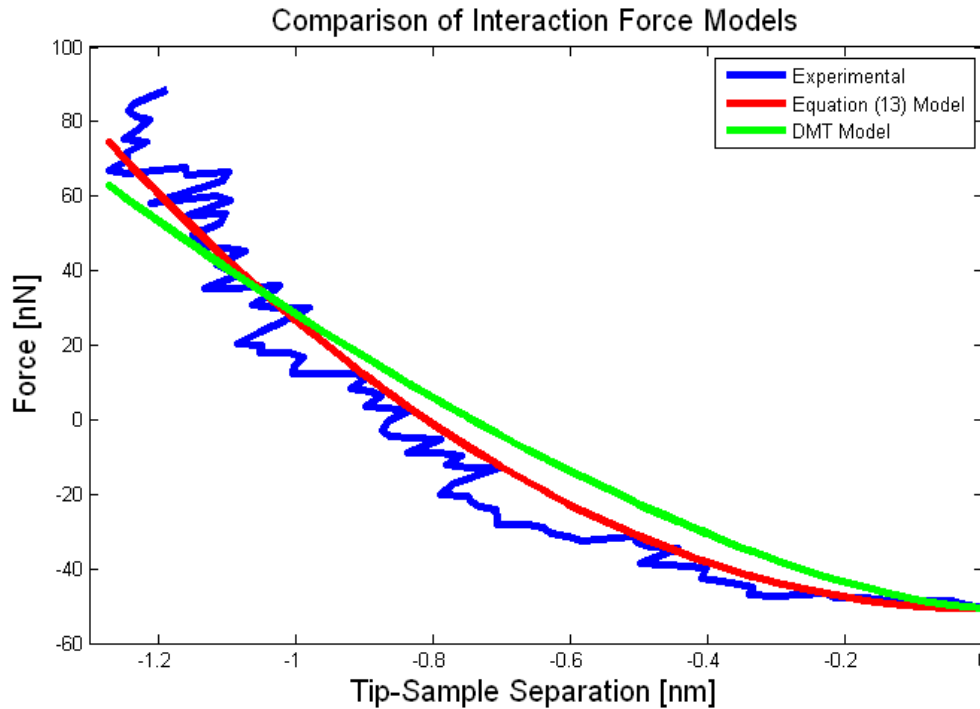
Figure A. 5 - Comparison of force curves.

The comparison of the three curves shows that equation (13) is a more accurate representation of the contact mechanics of this particular tip-sample interaction. However, force curves were only acquired for a few tip-sample combinations and the sample size is not sufficient to suggest that equation (13) is more accurate than the DMT model. Due to the relative inexperience in force curve acquisition within our research group, good repeatability in the force curves was not always accomplished, and in some cases the tip-sample interaction force parameters were well outside the expected range for the given tip-sample combination. Despite these issues, it was observed that for all force curves, the interaction force model from equation (13) provided a good representation of the experimental values, especially considering the fact that this simple piece-wise model is based on only two independent variables.

The insight gained from the this exploratory experimentation was also helpful in the initial experimental attempt to implement FFM and in being able to perform simulations using control schemes that would most closely resemble those that would be used in the eventual FFM operation. The author's most significant personal learning was that atomic force microscopes require a number of electronic instruments such as filters and lock-in amplifiers which cannot directly obtain and then adjust the frequency, phase, and amplitude at every oscillation, as was done in the simulations. Also, the forced method for achieving frequency modulation by resetting the excitation force after each oscillation in order to maintain maximum positive feedback, could not be performed experimentally.

The knowledge gained from performing the various experimentations was put to use in the first attempt towards experimental implementation of FFM through software modification of the MFP-3D operating system. A preexisting imaging mode developed by Asylum Research, referred to as SNAP mode, was altered for this implementation attempt. A pair of coupled feedback loops was created which maintained the 90 degree phase by adjusting the excitation frequency, and maintained the desired setpoint frequency by adjusting the excitation force amplitude. The modified SNAP mode had many limitations such as the fact that the sample had to be scanned in AC mode before being scanned in FFM mode, which defeated the purpose of using FFM to limit sample damage. The coupled feedback loops also failed to achieve the desired frequency shift and proved to be unstable when adjusting parameters such as the feedback loop gain values, setpoint values, scan speed, and scan size.

The failure of the software modification attempt at experimental implementation of FFM, along with increased knowledge of the atomic force microscope, led to the conclusion that a self-excitation mode was the most appropriate method of frequency-modulation implementation. The plan for the eventual experimental implementation of FFM is outlined in the Implementation of Self-Excitation section of the chapter on future work. The process of experimentally implementing FFM will be continued by the research group so that the findings of this paper, along with others on the benefits of FFM, can be verified experimentally.

References

[1] F. J. Giessibl. Forces and frequency shifts in atomic-resolution dynamic-force microscopy. *Physical Review B,* 56(24):16010-16015, **1997**.

[2] U. Dürig. Relations between interaction force and frequency shift in large-amplitude dynamic force microscopy. *Applied Physics Letters,* 75(3):433-435, **1999.**

[3] U. Dürig. Interaction sensing in dynamic force microscopy. *New Journal of Physics,* 2:5.1-5.12, **2000.**

[4] N. Sasaki and M. Tsukada. Theory for the effect of the tip-surface interaction potential on atomic resolution in forced vibration system of noncontact AFM. *Applied Surface Science,* 140:339-343, **1999.**

[5] A. I. Livshits, A. L. Shluger, A. L. Rohl, and A. S. Foster. Model of noncontact scanning force microscopy on ionic surfaces. *Physical Review B,* 59(3):2436-2448, **1999.**

[6] S. H. Ke, T. Uda, and K. Terakura. Quantity measured in frequency-shift-mode atomic-force microscopy: An analysis with a numerical model. *Physical Review B,* 59(20):13267-13272, **1999.**

[7] G. Binnig, C. F. Quate, and Ch. Gerber. Atomic Force Microscope. *Physical Review Letters,* 56(9):930-933, **1986.**

[8] A. Sasahara, S. Kitamura, H. Uetsuka, and H. Onishi. Oxygen-Atom Vacancies Imaged by a Noncontact Atomic Force Microscope Operated in an Atmospheric Pressure of N_2 Gas. *Journal of Physical Chemistry B,* 108:15735-15737, **2004.**

[9] I. Yu. Sokolov, G. S. Henderson, and F. J. Wicks. Theoretical and experimental evidence for "true" atomic resolution under non-vacuum conditions. *Journal of Applied Physics,* 86(10):5537-5540, **1999.**

[10] F. J. Giessibl. Atomic-Resolution of the Silicon (111)-(7x7) Surface by Atomic-Force Microscopy. *Science,* 267:68-71, **1995.**

[11] K. Yamanaka, A. Noguchi, T. Tsuji, T. Koike, and T. Goto. Quantitative Material Characterization by Ultrasonic AFM. *Surface and Interface Analysis,* 27:600-606, **1999.**

[12] B. Deng, X. Yan, Q. Wei, and W. Gao. AFM characterization of nonwoven material functionalized by ZnO sputter coating. *Materials Characterization,* 58:854-858, **2007.**

[13] R. García, R. Magerle, and R. Perez. Nanoscale compositional mapping with gentle forces. *Nature Materials,* 6:405-411, **2007.**

[14] R. G. Winkler, J. P. Spatz, S. Sheiko, M. Möller, P. Reineker, and O. Marti. Imaging material properties by resonant tapping-force microscopy: A model investigation. *Physical Review B,* 54(12):8908-8912, **1996.**

[15] D. Tranchida, S. Piccarolo, and Maria Soliman. Nanoscale Mechanical Characterization of Polymers by AFM Nanoindentations: Critical Approach to the Elastic Characterization. *Macromolecules*, 39:4547-4556, **2006.**

[16] T. Junno, K. Deppert, L. Montelius, and L. Samuelson. Controlled manipulation of nanoparticles with an atomic force microscope. *Applied Physics Letters,* 66(26):3627-3629, **1995.**

[17] R. García, M. Calleja, and F. Pérez-Murano. Local oxidation of silicon surfaces by dynamic force microscopy: Nanofabrication and water bridge formation. *Applied Physics Letters,* 72(18):2295-2297, **1998.**

[18] Y. Martin, C. C. Williams, and H. K. Wickramasinghe. Atomic force microscope-force mapping and profiling on a sub 100-Å scale. *Journal of Applied Physics,* 61(10):4723-4729, **1987.**

[19] R. García and A. San Paulo. Attractive and repulsive tip-sample interaction regimes in tapping-mode atomic force microscopy. *Physical Review B,* 60(7):4961-4967, **1999.**

[20] M. Marth, D. Maier, J. Honerkamp, R. Brandsch, and G. Bar. A unifying view on some experimental effects in tapping-mode atomic force microscopy. *Journal of Applied Physics,* 85(10):7030-7039, **1999.**

[21] A. San Paulo and R. García. Unifying theory of tapping-mode atomic-force microscopy. *Physical Review B,* 66:041406(4), **2002.**

[22] R. García and R. Pérez. Dynamic atomic force microscopy methods. *Surface Science Reports,* 47:197-301, **2002.**

[23] T. R. Albrecht, P. Grütter, D. Horne, and D. Rugar. Frequency modulation detection using high-Q cantilevers for enhanced force microscope sensitivity, *Journal of Applied Physics,* 69(2):668-673, **1991.**

[24] B. V. Derjaguin, V. M. Muller, and Y. P. Toporov. Effect of Contact Deformations on Adhesion of Prticles. *Journal of Colloid and Interface Sciences,* 53(2):314-326*,* **1975**

[25] N. A. Burnham and A. J. Kulik. Surface Forces and Adhesion. Appearing in *Handbook of Micro/Nanotribology, second edition,* B. Bhushan, ed.. CRC Press, Boca Raton, FL, **1999.**

[26] K. Yagasaki. Nonlinear dynamics of vibrating microcantilevers in tapping-mode atomic force microscopy. *Physical Review B,* 70(24):245419(10), **2004.**

[27] N. A. Burnham, R. J. Colton, and H. M. Pollock. Interpretation issues in force microscopy. *Journal of Vacuum Science and Technology A,* 9(4):2548-2556, **1991.**

[28] K.L Johnson, K. Kendall, and A. D. Roberts. Surface Energy and Contact of Elastic Solids. *Proceedings of the Royal Society of London Series A-Mathematical and Physical Sciences,* 324(1558):301-313, **1971.**

[29] D. Maugis. Adhesion of Spheres – The JKR-DMT transition using a Dugdale model. *Journal of Colloid and Interface Science,* 150(1):243-269, **1992.**

[30] F. J. Giessibl. Advances in atomic force microscopy. *Reviews of Modern Physics,* 75(3):949-983, **2003.**

[31] Y. Song and B. Bhushan. Atomic force microscopy dynamics modes: modeling and applications. *Journal of Physics: Condensed Matter,* 20:225012(29), **2008.**

[32] J. H. Cantrell and S. A. Cantrell. Analytical model of the nonlinear dynamics of cantilever tip-sample surface interactions for various acoustic atomic force microscopes. *Physical Review B,* 77(16):165409(16), **2008.**

[33] G. Y. Chen, R. J. Warmack, A. Huang, and T. Thundat. Harmonic response of near-contact scanning force microscopy. *Journal of Applied Physics,* 78(3):1465-1469, **1995.**

[34] B. Anczykowski, D. Krüger, and H. Fuchs. Cantilever dynamics in quasinoncontact force microscopy: Spectroscopic aspects, *Physical Review B,* 53(23):15485-15488, **1996.**

[35] L. Wang. Analytical description of the tapping-mode atomic force microscopy response. *Applied Physics Letters,* 73(25):3781-3783, **1998.**

[36] H. Hölscher, B. Gotsmann, W. Allers, U. D. Schwarz, H. Fuchs, and R. Wiesendanger. Measurement of conservative and dissipative tip-sample interaction forces with dynamic force microscope using frequency modulation technique. *Physical Review B,* 64(7):075402(6), **2001.**

[37] S. D. Solares. Single Biomolecule Imaging with Frequency and Force Modulation in Tapping-Mode Atomic Force Microscopy. *Journal of Physical Chemistry B Letters,* 111(9):2125-2129, **2007.**

[38] S. D. Solares. Eliminating bistability and reducing sample damage through frequency and amplitude modulation in tapping-mode atomic force microscopy. *Measurement Science and Technology,* 18(3):592-600, **2007.**

[39] S. D. Solares. Frequency and Force modulation atomic force microscopy: low-impact tapping-mode imaging without bistability, *Measurement Science and Technology,* 18(7):L9-L14, **2007.**

[40] S. D. Solares and J. C. Crone. Real-time simulation of isolated biomolecule characterization with frequency and force modulation atomic force microscopy. *Journal of Physical Chemistry C,* 111(27):10029-10034, **2007.**

[41] Y. C. Guo, X. F. Zhou, J. L. Sun, M. Q. Li, and J. Hu. Height measurements of DNA molecules with lift mode AFM. *Chinese Science Bulletin,* 49(15):1574-1577, **2004**

[42] R. Godehardt, W. Lebek, R. Adhikari, M. Rosenthal, C. Martin, S. Frangov, and G. Michler. Optimum topographical and morphological information in AFM tapping mode investigation of multicomponent polyethylene. *European Polymer Journal,* 40:917-926, **2004.**

[43] J. V. Macpherson and P. R. Unwin. Noncontact Electrochemical Imaging with Combined Scanning Electrochemical Atomic Force Microscopy. *Analytical Chemistry,* 73(3):550-557, **2001.**

[44] Oakdale Engineering. DataFit version 9.0.59. **2008.**

[45] S. Scheuring, J. Seguin, S. Marco, D. Levy, C. Breyton, B. Robert, and J. L. Rigaud. AFM characterization of tilt and intrinsic flexibility of Rhodobacter sphaeroides light harvesting complex 2 (LH2), *Journal of Molecular Biology,* 325(3):569-580, **2003.**

[46] M. Hegner and A. Engel. Single Molecule Imaging and Manipulation. *CHIMIA,* 56(10):506-514, **2002.**

[47] C. Moller, M. Allen, V. Elings, A. Engel, and D. J. Muller. Tapping-mode atomic force microscopy produces faithful high-resolution images of protein surfaces, *Biophysical Journal,* 77(2):1150-1158, **1999.**

[48] S. Karrasch, R. Hegerl, J. H. Hoh, W. Baumeister, and A. Engel. Atomic force microscopy produces faithful high-resolution images of protein surfaces in an

aqueous environment. *Proceedings of the National Academy of Sciences of the United States of America,* 91(3):836-838, **1994.**

[49] A. Engel and D. J. Muller. Observing single biomolecules at work with the atomic force microscope. *Nature Structural Biology,* 7(9):715-718, **2000.**

[50] L. Verlet. Computer "Experiments" on Classical Fluids. I. Thermodynamical Properties of Lennard-Jones Molecules. *Physical Review,* 159(1):98-103, **1967.**

[51] S. Morita and Y. Sugawara. Guidelines for the achievement of true atomic resolution with noncontact atomic force microscopy. *Applied Surface Sciences,* 140:406-410, **1999.**

[52] S. D. Solares and G. Chawla. Dual frequency modulation with two cantilevers in series: a possible means to rapidly acquire tip-sample interaction force curves with dynamic AFM. *Measurement Science and Technology,* 19(5):055502(8), **2008.**

[53] S. D. Solares. Characterization of deep nanoscale surfaces trenches with AFM using thin carbon nanotube probes in amplitude-modulation and frequency-force-modulation modes. *Measurement Science and Technology,* 19:015503(10), **2007.**

[54] I. R. Shapiro, S. D. Solares, M. J. Esplandiu, L. A. Wade, W. A. Goddard, and C. P. Collier. Influence of Elastic Deformation on Single-Wall Carbon Nanotube Atomic Force Microscopy Probe Resolution. *Journal of Physical Chemistry B,* 108:13613-13618, **2004.**

[55] G. Binnig and H. Rohrer. In touch with atoms. *Reviews of Modern Physics,* 71:S324-S330, **1999.**

[56] T. R. Ramachandran, C. Baur, A. Bugacov, A. Madhukar, B. E. Koel, A. Requicha, and C. Gazen. Direct and controlled manipulation of nanometer-sized particles using the non-contact atomic force microscope. *Nanotechnology,* 9(3):237-245, **1998.**

[57] A. Checco, O. Gang, and B. M. Ocko. Liquid Nanostripes. *Physical Review Letters,* 96:056104(4), **2006.**

[58] S. D. Solares, M. J Esplandiu, W. A. Goddard, and C. P. Collier. Mechanisms of Single-Walled Carbon Nanotube Probes-Sample Multistability in Tapping Mode AFM Imaging. *Journal of Physical Chemistry B,* 109(23):11493-11500, **2005.**

[59] P. Budau. Self-driven flexible string. *Physics Letters A,* 317:252-254, **2003.**

[60] F. J. Giessibl and M. Tortonese. Self-oscillating mode for frequency modulation noncontact atomic force microscopy. *Applied Physics Letters,* 70(19):2529-2531, **1997.**

[61] T. Itoh and T. Suga. Deflection detection and feedback actuation using a self-excited piezoelectric Pb(Zr,Ti)O3 microcantilever for dynamic scanning force microscopy. *Applied Physics Letters*, 69(14):2036-2038, **1996**.

[62] M. Labardi. Stability of dynamic force microscopy with the self-oscillator method. *Nanotechnology,* 17:3071-3080, **2006.**